Theses and Dissertations

Fall 2010

Multiscale modeling and simulation of material phase change problems: ice melting and copper crystallization

Xiupeng Wei
University of Iowa

Recommended Citation

Wei, Xiupeng. "Multiscale modeling and simulation of material phase change problems: ice melting and copper crystallization." MS (Master of Science) thesis, University of Iowa, 2010.
http://ir.uiowa.edu/etd/904.

MULTISCALE MODELING AND SIMULATION

OF MATERIAL PHASE CHANGE PROBLEMS:

ICE MELTING AND COPPER CRYSTALLIZATION

by

Xiupeng Wei

A thesis submitted in partial fulfillment
of the requirements for the Master of Science
degree in Mechanical Engineering
in the Graduate College of
The University of Iowa

December 2010

Thesis Supervisor: Associate Professor Shaoping Xiao

Graduate College
The University of Iowa
Iowa City, Iowa

CERTIFICATE OF APPROVAL

_____

MASTERØS THESIS

_____

This is to certify that the Masterøs thesis of

Xiupeng Wei

has been approved by the Examining Committee
for the thesis requirement for the Master of Science degree
in Mechanical Engineering at the December 2010 graduation.

Thesis Committee: _____
                   Shaoping Xiao, Thesis Supervisor

                   _____
                   Albert Ratner

                   _____
                   Olesya I. Zhupanska

ACKNOWLEDGMENTS

I am very grateful to my advisor, Professor Shaoping Xiao, for his suggestions and careful guidance throughout my graduate studies. I really appreciate his excellent and professional advices.

I would also like to thank Professor Jun Ni. His support and professional guidance were very helpful for the completion of this work.

I would also like to thank Professor Albert Ratner and Professor Olesya I. Zhupanska for their willingness to be on my thesis defense committee and review my graduate research work. I appreciate their valuable comments.

ABSTRACT

The primary objective of this work is to propose a state-of-the-art physics based multiscale modeling framework for simulating material phase change problems. Both ice melting and copper crystallization problems are selected to demonstrate this multiscale modeling and simulation. The computational methods employed in this thesis include: classical molecular dynamics, finite element method, phase-field method, and multiscale (nano/micro coupling) methods.

Classical molecular dynamics (MD) is a well-known method to study material behaviors at atomic level. Due to the limit of MD, it is not realistic to provide a complete molecular model for simulations at large length and time scales. Continuum methods, including finite element methods, should be employed in this case.

In this thesis, MD is employed to study phase change problems at the nanoscale. In order to study material phase change problems at the microscale, a thermal wave method one-way coupling with the MD and a phase-field method one-way coupling with MD are proposed. The thermal wave method is more accurate than classical thermal diffusion for the study of heat transfer problems especially in crystal based structures. The second model is based on the well-known phase-field method. It is modified to respond to the thermal propagation in the crystal matrix by the thermal wave method, as well as modified to respond to temperature gradients and heat fluxes by employing the Dual-Phase-Lag method. Both methods are coupled with MD to obtain realistic results.

It should be noted that MD simulations can be conducted to obtain material/thermal properties for microscopic and/or macroscopic simulations for the purpose of hierarchical/sequential multiscale modeling. These material parameters include thermal conductivity, specific heat, latent heat, and relaxation time. Other type of interfacial parameters that occur during the phase change process, such as nucleus shape,

interfacial energy, interfacial thickness, etc., are also obtained by MD simulation since these have so far been too difficult to measure experimentally.

I consider two common phase change phenomena, ice melting and copper crystallization, in this thesis. For the case of ice melting, MD is first employed to study its phase change process and obtain thermal properties of ice and water. Several potential models are used. I conduct simulations of both bulk ice and ice/water contacting cases. It is found that various potential models result in similar melting phenomena, especially melting speed. Size effects are also studied and it is found that the melting time is longer for larger bulk ice segments but that the average melting speed is size dependent. There is no size effect for the melting speed at ice/water interface at the nanoscale if the same temperature gradient is applied. The melting speed of ice should depend on the temperature gradient. To study ice melting at the microscale, the thermal wave model is employed with parameters obtained from MD simulations. It is found that ice melting speed is scale, for both length scale and time scale, dependent.

For the case of copper crystallization, an EAM potential is first employed to conduct MD simulations for studying the copper crystallization process at the nanoscale. I obtain thermal properties and interfacial parameters, including thermal diffusion coefficient, latent heat, relaxation time, interfacial thickness, interfacial energy and the anisotropy coefficients, and nucleus shape etc. A central symmetry parameter is used to identify an atom in solid state or liquid state. And then an initial nucleus shape is obtained and used as the input for microscale simulation, in which the phase-field method is used to study copper crystallization at the microscale.

TABLE OF CONTENTS

LIST OF TABLES

LIST OF FIGURES

CHAPTER 1

INTRODUCTION

1.1 Motivations

Phase change problems, including melting and solidification, are very important in many engineering applications such as the freezing of food, metal processing, and solidification of castings.

Recently, nano-materials and devices with desirable structures have become a promising field with the development of nanotechnology. In order to manufacture new nanomaterials, it is important to understand the underlying mechanisms of material formation. These processes involve chemical and physical effects including: 1) The early stage of nucleation due to supercooling; 2) The transitional stage of nanocrystallization in terms of nanocrystal patterns, growth orientations, growth rates, liquid/solid interface microstructure, and interface topology; 3) The late stage of nanocrystal growth and nanoparticle/crystal formation; and 4) The final stage of solid-state phase transitions and final physical, chemical and mechanical heterogeneities. All of those stages influence the final material properties. For example, the microscopic size and shape of nanocrystal will determine the final thermal properties and failure characteristics. Therefore, it is a critical need to simulate the phase change processes of nanomaterials at both nano and micro scales in order to control and predict the resulting material properties.

Many efforts have been devoted to the study of phase change mechanisms. However, the details of phase change processes are not yet fully understood. For example, most microscale numerical methods assume that interfacial thickness is constant. However, it is still not clear what the interfacial thickness is for a given material at a supercooling condition. Although phase change mechanisms can be observed at the nanoscale via MD simulations, it is difficult to predict the phase change phenomena at larger length and time scales due to the inherent limitations of MD. On the other hand,

the conventional phase-field method for phase change problems employs the classical thermal diffusion equation, which is considered to describe macroscopic behaviors over many grains during at long time scales. It is obviously not proper to use the thermal diffusion equation at the microscale.

At the present time, researchers study phase change problems at either nanoscale or microscale. No work has yet coupled these two scales. This challenge motivates me to study the mechanisms of phase change problems in a multiscale-based manner.

In this thesis, two phase change problems are considered. One is ice melting, and the other is copper crystallization. MD and conventional phase field method, the following methods are developed and employed in this thesis:

a) A thermal wave model replaced the thermal diffusion model is one-way coupled with MD via employing the parameters obtained from MD simulations.

b) A multiscale based phase-field method, which also uses thermal parameters obtained from MD simulation. In addition, the interfacial parameters such as interfacial thickness, initial nucleus shape which are often assumed in current research are calculated from MD simulation. This multiscale one-way coupling method thus improves computational accuracy at the microscale as compared with classical phase change simulations.

1.2 Objective of the study

The primary goal of this work is to provide a state-of-the-art, multiscale-based framework to model and simulate material phase change problems, including ice melting and copper crystallization, at the nano/microscales. The goal can be achieved with the following objectives:

1) Conduct MD simulations to simulate phase change problems of ice melting and copper crystallization.

2) Calculate thermal properties and interfacial parameters via MD simulations.

3) Couple the thermal wave method with MD simulations to study ice melting at the microscale.

4) Develop the phase-field method one-way coupling with MD results to study copper crystallization at the microscale.

To the author's knowledge, there's no existing or finished integrated project which intends to accomplish all of the above tasks. In this thesis, the above objectives are accomplished via MD simulations and the new multiscale simulation methods developed here. The model and methods developed in this thesis can be easily extended to other materials and other phase change problems.

1.3 Contents of the thesis

In Chapter 2, I present the scientific background and the literature review of phase change problems. The research on phase change problems simulated via conventional numerical methods at the macroscale and microscale as well as the classical MD method at the nanoscale are also reviewed.

In Chapter 3, the methodologies to model and simulate phase change problems at the nano/microscale are presented. At the nanoscale, MD is described. Then the techniques for how to calculate thermal properties and interfacial parameters via MD simulations are presented. Next a multiscale method in which the thermal wave method is employed to study phase change problems at the microscale while the intrinsic parameters are obtained via MD simulations is proposed. In addition, a multiscale-based phase-field to study nucleus growth during copper crystallization is developed.

MD simulations are first conducted to study ice melting process at the nanoscale in Chapter 4. Various potential functions are employed in similar melting process for both ice bulk and ice/water contacting. Then the proposed thermal wave method is used to study ice melting at the microscale and compared the speed with the ones at the nano and macro scales.

In Chapter 5, MD simulations are first conducted to study copper crystallization at the nanoscale. The thermal properties and interfacial parameters are obtained and then used as input parameters for my developed multiscale-based phase-field model. The results are compared with MD simulation and macroscale results.

Chapter 6 presents the summaries and conclusions. Recommendations of future work are also presented.

CHAPTER 2

LITERATURE REVIEW

2.1 Material phase change problems

A phase change is the transformation of a material from one phase or state of matter to another phase or state. It includes phase changes between solid, liquid and gaseous states of matter. Figure 2.1 shows an often observed phenomenon, ice melting. During a phase change process of a given material, several properties of the material will change as a result of external conditions, including temperature, pressure and others. The measurement of the external conditions at which the transformation occurs, is termed as the phase transition point. For example, the melting point of a solid is the temperature at which a solid can transform to a liquid.

Figure 2.1 Ice melting phenomenon in nature

Source: UNIONGAS, www.uniongas.com

Since phase change problems are often seen phenomena in nature and are very important in engineering applications, significant efforts have been made to elucidate the physical processes. Here, a review of analytical solutions and numerical methods for this type of problems at the macroscale is presented, as well as numerical methods including phase-field and level set methods at the microscale and MD at the nanoscale.

2.1.1 Analytical solution at the macroscale

Initially, macroscale simulations of phase change problems focused on how to obtain analytical solutions. Early analytical methods were proposed by Lame and Clapeyron [1] in 1831 and Stefan [2] in 1891, to describe ice formation. The simplest phase change problem is a one-phase problem first solved analytically by Stefan [2]. Therefore, a phase change problem is often called as Stefan problem.

Neumann [3] extended Stefanøs solution to the two-phase problem, which is more realistic for phase change problems. Figure 2.2 illustrates the two-phase problem clearly.
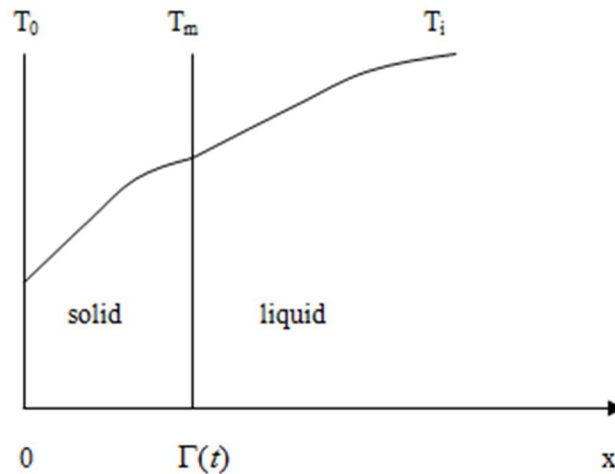
Figure 2.2 Solidification in a half space for the two phase problem

In the case described by Figure 2.2, a liquid at a uniform temperature T_i, that is higher than the melting temperature T_m, is confined to a half space. The liquid/solid interface is at $\Gamma(t)$, existing at the melting temperature. A constant temperature T_0 below T_m, is imposed on the face at $x = 0$. With assumptions of constant material properties, the problem can be mathematically expressed as follows:

$$\frac{\partial T}{\partial t} = \alpha \frac{\partial^2 T}{\partial x^2}, \ x \in \Omega \ (t) \tag{2.1}$$

$$T = T_m, \ x \in \Gamma(t) \tag{2.2}$$

$$k_s \frac{\partial T_s}{\partial x}\bigg|_{x=\delta(t)} - k_l \frac{\partial T_l}{\partial x}\bigg|_{x=\delta(t)} = \rho_s L_f \frac{d\Gamma}{dt}, \ x \in \Gamma(t) \tag{2.3}$$

where T is the temperature field, α is the thermal diffusivity, k is the thermal conductivity, ρ is the density of material, L_f is the latent heat of fusion, Ω is the simulation domain including solid and liquid phases, and subscript s and l donate solid and liquid phases.

Equation (2.1) is the thermal diffusion equation. Equation (2.2) is the enforced condition at the phase change interface, and Equation (2.3) expresses the release or absorption of the latent heat at the interface.

By assuming the solution in solid and liquid phases in a certain form and defining the interface position as $\Gamma(t) = 2\lambda(\alpha_s t)^{1/2}$, Neumann [3] obtained the exact solution by solving the coupled Equations (2.1) to (2.3). The solution has an explicit expression for the temperature distributions in both solid and liquid phases, respectively, shown in Equations (2.4) and (2.5), where the coefficient λ is calculated through Equation (2.6).

$$\frac{T_l - T_i}{T_m - T_i} = \frac{erf[x/2(\alpha_l t)^{1/2}]}{erf(\lambda)} \tag{2.4}$$

$$\frac{T_s - T_0}{T_m - T_0} = \frac{erfc[x/2(\alpha_s t)^{1/2}]}{erfc[\lambda(\alpha_l/\alpha_s)^{1/2}]} \tag{2.5}$$

$$\frac{e^{-\lambda^2}}{erf(\lambda)} + \frac{k_s}{k_l}(\frac{\alpha_l}{\alpha_s})^{1/2}\frac{T_m - T_0}{T_i - T_m}\frac{e^{-\lambda^2(\alpha_l/\alpha_s)}}{erfc[\lambda(\alpha_l/\alpha_s)^{1/2}]} = \frac{\lambda L_f \sqrt{\pi}}{C_{Pl}(T_i - T_m)} \tag{2.6}$$

However, Neumann's solution is available only for phase change problems in the rectangular coordinate systems. For phase change problems in the cylindrical coordinate system, Paterson [4] had shown the exact solution can be expressed as an exponential integral function. Equations (2.7) and (2.8) show the temperatures in the solid and liquid phases, respectively. The constant λ is determined from transcendental equation (2.9). The solid/liquid interface position is formulated the same as the one in Neumann's exact solution.

$$T_s = T_m - \frac{Q}{4\pi k_s}[Ei(-\frac{r^2}{4\alpha_s t}) - Ei(-\lambda^2)] \tag{2.7}$$

$$T_l(r,t) = T_i - \frac{T_i - T_m}{Ei(-\lambda^2\alpha_s/\alpha_l)}Ei(-\frac{r^2}{4\alpha_l t}) \tag{2.8}$$

$$-\frac{Q}{4\pi}e^{-\lambda^2} + \frac{k_l(T_i - T_m)}{Ei(-\lambda^2\alpha_s/\alpha_l)}e^{-\lambda^2\alpha_s/\alpha_l} = \lambda^2\alpha_s\rho L_f \tag{2.9}$$

where Q is a line heat source of strength located at $r = 0$, Ei is an exponential integral function, and r is the radius of the cylinder.

It should be noted that exact solutions only exist for semi-infinite problems. There is no exact solution available for the melting or solidification of a slab with a finite thickness. Therefore, the integral method must be used to obtain approximated solutions for such problems including heat flux boundary conditions without constant temperatures. The integral method, which dates back to von Karman and Pohlhausen, who used it to solve boundary layer equations, was applied by Goodman [5] to solve a one dimensional transient melting problem. It was subsequently employed by many researchers [6-9] for solving various types of one-dimensional phase change problems. This method provides a relatively straightforward and simple approach to phase change problems. The method is outlined below:

a) Assume that the temperature distribution depends on the spatial variable in a particular form which is consistent with the boundary condition. The assumed solution, for example, could be a polynomial approximation;

b) Integrate the heat conduction equation with respect to the spatial variable over the appropriate interval and substitute the assumed form of the temperature distribution to attain the heat balance integral;

c) Solve the integral equation to obtain the solutions for temperature distribution and moving boundaries.

Goodman [5] used this method to solve a single phase ice melting problem and two phase slab solidification problems. The approximated solutions they obtained were quite good when compared with exact solutions. The integral method has been extensively applied to different problems; however, the mathematical manipulations for complex problem can be very complicated and cumbersome. Moreover, selecting a satisfactory approximation to the temperature distribution is a major difficulty in this method. For example, the use of a high order polynomial makes very complicated analysis, and even does not necessarily improve the accuracy of the solution.

2.1.2 Numerical methods at the macroscale

When analytical methods are not available, numerical methods can be used to solve the phase change problems. Finite difference methods (FDM) and Finite element methods (FEM) are two popular techniques for numerical analysis. Each has its own advantages and disadvantages. With the development of more advanced and powerful computers, more sophisticated numerical models have been developed to handle multidimensional problems with very complex geometries.

A fixed grid method [6- 12] (for both FEM and FDM) was developed to conduct numerical analyses. In this method, the space and time domains are subdivided into finite number of equal grids with Δx, Δt during the simulations, as illustrated in Figure 2.3.

The moving solid/liquid interface will in general lies somewhere between two grids at any given time steps. The new temperature is updated from temperatures of the previous time step on the basis of the following formulation:

$$T_{ib,n+1} = T_{ib,n} + (\frac{\Delta t}{\Delta x^2})(T_{ib-1,n} - 2T_{ib,n} + T_{i+1,n})$$ (2.10)
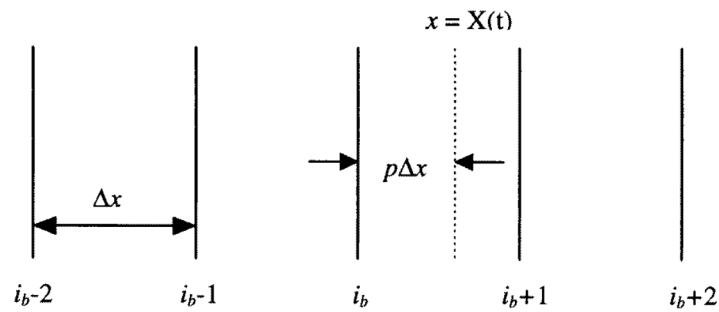
Figure 2.3 Illustration of fixed grid method

Crank [6] used this method to estimate the location of the interface by a suitable three point Lagrange interpolation formula shown as following:

$$T_{ib,n+1} = T_{ib,n} + (\frac{2\Delta t}{\Delta x^2})(\frac{1}{p_n+1}T_{ib-1,n} - \frac{1}{p_n}T_{ib,n})$$ (2.11)

$$p_{n+1} = p_n - (\frac{\Delta t}{\rho L_f \Delta x^2})(\frac{p_n}{p_n+1}T_{ib-1,n} - \frac{1}{p_n}T_{ib,n})$$ (2.12)

It should be noted that the above numerical solutions were obtained by FDM. C.K. Chun [10] used this method with an implicit time integration to solve phase change problems and obtained excellent solutions.

FEM with fixed grids were also widely used by researchers. Boris [11] used a FEM to solve one dimensional phase change problem, and E. Feulvarch [12] presented an implicit fixed grid method for the finite element analysis of phase change problems.

The major advantage of fixed grid method is that it can handle multidimensional problem efficiently without many difficulties. However, this method may sometimes be unstable when the boundary moves a distance larger than a space increment in a time step. Therefore, the variable grid method was developed to avoid the problems associated with the fixed grid method.

In the variable grid method, the space or time domain is subdivided into equal intervals in one direction only and the corresponding grid side in the other direction is determined so that the moving boundary (i.e. the solid/liquid phase interface) always remains at a grid point.

The variable grid method based on the variable space grids, also known as the dynamic grids, where the time step Δt is unique in the time domain. The number of spatial intervals is fixed. However, the spatial intervals are adjusted so that the moving boundary lies on a particular grid point. Murray and Landis [13] used this method to solve a phase change problem based on below equation:

$$\frac{dT}{dt}\bigg|_{i} = \frac{x}{\delta(t)}\frac{d\delta}{dt}\frac{\partial T}{\partial x} + \frac{\partial^2 T}{\partial x^2} \qquad (2.13)$$

Another variable method has various time steps. In this method, the space domain is subdivided into fixed equal interval Δx, while the time step varies. The interface moves with a distance Δx during the time interval Δt, and always remains at a grid point at the end of each time interval. Douglas and Gallie [14] used this method to solve some phase change problems. Several variations of a variable time step method have been reported by [6, 15].

The enthalpy method has been used by several researchers to solve phase change problems in which the material doesnot have a distinct solid/liquid interface. Instead, the melting or solidification takes place over an extended range of temperatures. The solid and liquid phases are separated by a two phase moving region. In this approach, an enthalpy function is used as dependent variable along with the temperature. The heat conduction equation in this method is as follows:

$$\rho \frac{\partial h}{\partial t} = \nabla \cdot (k \nabla T) \qquad (2.14)$$

where ρ is the density of the material, h is the enthalpy, k is the thermal conductivity of the material, and T is the temperature.

The enthalpy method treats the enthalpy as an unknown and uses either an explicit method or an iterative implicit method to solve the above equation. The relationship between the enthalpy and the temperature can be defined in terms of the latent heat release characteristics of the phase change material. It always assumed to be a step function for isothermal phase change and a linear function for non-isothermal problems.

Cames [16] used this method for isothermal phase change problems. Tamma [17] recently used an explicit enthalpy method in FEM. Thevoz [18] has used an implicit enthalpy method to solve phase change problems.

There are inherent drawbacks in both variable methods and enthalpy methods. Various grid methods have a common issue of grid generation for complex interfaces. The difficulties increase with the dimension of the problem. Although enthalpy methods do not need remeshing, it cannot accurately model materials with an isothermal phase change if there is a mushy zone instead of a sharp interface between solid and liquid.

During last ten years, the extended finite element method (XFEM),which is an extension of the methods presented by Belytschko et al [19,20], has been used to solve phase change problems. The basic idea of XFEM approaches is to explicitly track the interface and to construct enriched finite element spaces depending on the interface

position while keeping the mesh fixed. R. Merle and J. Dolbow [21] first attempted to use XFEM to solve thermal and phase change problems. It allowed them obtained accurate solutions on fixed finite element meshes as there were no concerns about element distortion. Jack Chessa et al [22] extended this method enriched with the enrichment of a discontinuity in the derivative of the temperature normal to the interface. Their numerical examples showed this method is quite stable and free of oscillations along the phase interface.

2.2 Phase-field method for material phase change problems

Within recent 40 years, solving phase change problems at the microscale has become a topic of extensive research [23, 24]. Many mathematical models were developed to study the microscopic structure as well as nucleation and crystal growth during the phase change process.

One popular approach is to use phase-field method, which has made a significant progress. In this method, an imagery phase-field variable θ is defined as the function of time and the interface position. The phase-field variable is introduced to describe whether the material is phase changed or not, i.e., solid or liquid. This variable is governed by a phase-field control equation that is coupled to heat equation. The interface between solid and liquid is described by the phase-field variable that smoothly changes between 0 and 1, which represent solid and liquid phases respectively. Important physical mechanisms during phase change processes, such as curvature, anisotropy and kinetics effects, are implicitly incorporated in the phase-field control equation. This results in many computational advantages. The typical phase-field model for pure material is:

$$\rho c_v T_t + \frac{L_f}{2} \theta_t = k \Delta T \qquad (2.15)$$

$$\alpha \varepsilon^2 \theta_t = \varepsilon^2 \Delta \theta - F_\theta(\theta, T) \qquad (2.16)$$

Equation (2.15) is a modified thermal diffusion equation and Equation (2.16) is the phase equation, where ε is the thickness of the interface like shown in Figure 2.4, $F(\theta,u)$ is the free energy density function to describe the solid and liquid phases which can take on many forms, ρ is the density of the material, c_v is the specific heat, T is the temperature distribution, L_f is he latent heat of fusion, k is the thermal conductivity, and α is the relaxation scaling.
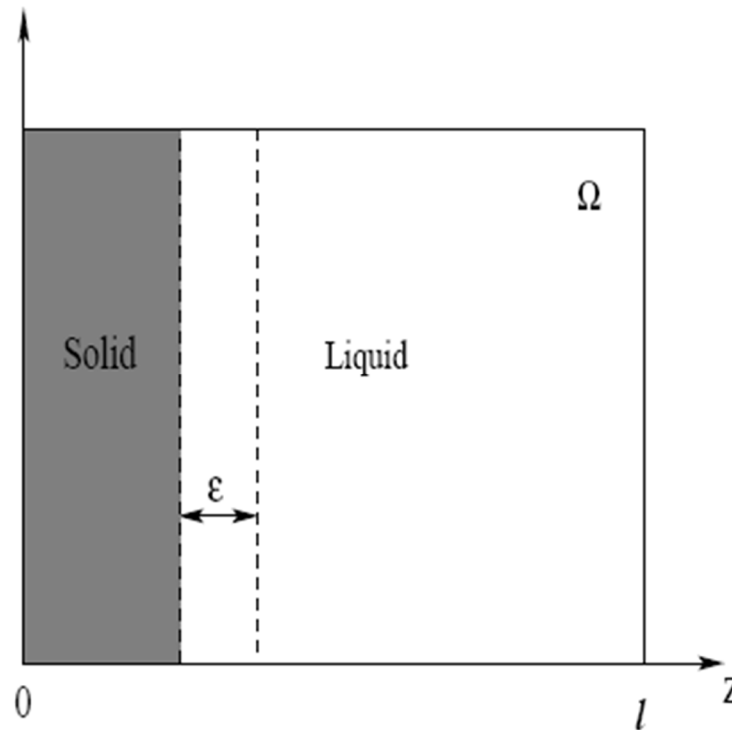
Figure 2.4 Illustration of the phase-field model in one-dimension

The phase-field method is usually constructed in such a way that in the limit of small interface width the correct interfacial dynamics is recovered. This approach permits

to solve the problem by integrating a set of partial differential equations for all the system, thus avoiding the explicit treatment of the boundary conditions at the interface.

This phase-field model was first introduced by Fix [25] and Langer [26], and has been experienced a growing interest in solidification and other areas. Caginalp and Fife [27] proposed a phase-field model that introduced surface tension and other important interfacial parameters. They found that the classical phase change problems (sharp interface problems) could be recovered mathematically by using the phase-field approach as a numerical method to smooth solution over a thin interface with finite interfacial thickness, in which effects of surface tension and supercooling were included. In addition, Penrose and Fife [28] derived a thermodynamically consistent phase-field model, and Wang et al. [29] presented this model based on the first and second thermal dynamics laws. The overview of this method for phase change problems can be found in Boettinger et al [30].

The major pro of the phase-field method is that it can avoid to first distinguishing the boundaries of interface mathematically. Indeed, the interface can be obtained from the numerical solution for the phase-field variable. One of the cons of the phase-field method is the significant computational effort required, especially when investigating dendritic growth in the presence of convection and multiple array dendritic growth. However, it can be improved by using the techniques of adaptive gridding and parallel computation. Another con is related to the large number of parameters involved in the governing equations. These parameters are difficult to determine for accurate physical crystal growth simulation of real materials.

2.3 Level set method for material phase change problems

Another alternative approach is to use the level set method, which was first introduced by Osher et.al. [31]. It has been applied to elucidate many physical phenomena [32]. In this method, the interface is described by a level set variable ϕ, which

equals to 0 at the solid-liquid interface. Indeed, the interface is always represented by the zero level set of a smooth, continuous function. The main advantage of the level set method is that the interface is never explicitly tracked and complicated interface topology can be easily represented. The interface front is advanced by solving the level set equation:

$$\phi_t + \vec{v} \cdot \nabla \phi = 0 \tag{2.17}$$

where $\vec{v}$ is the velocity field. The phase changed materials and unchanged materials are represented by the value where $\phi < 0$ and $\phi > 0$ respectively.

A simple level set method was proposed by Chen et.al. [32]. They used an implicit time discretization method to keep tracking the interface and to solve the thermal diffusion field. However, their method is limited to one and two dimensional cases. Kim [33] extended this method in a more accurate manner and obtained results in excellent agreement with the predictions of microscopic solvability theory. However, both of methods were lack of symmetry and made this approach computationally expensive. In addition, they directly applied temperature boundary conditions on the interface as well as the computation of heat fluxes from the temperature nodal values. This usually leaded to energy conservation issues associated with the discretization error. It may result in large variation of the results if different sizes and orientations of mesh are used.

Tan and Zabaras [34] recently used the level set method combining features of front-tracking and fixed domain methods to study dendritic solidification phase change problems. The computed results agree very well with available analytical solutions as well as with the ones obtained via front-tracking techniques. Wang et al [35] conducted simulations by parallelizing level set method to study phase change problems. Numerical results were reported to demonstrate the advantages of using their method.

2.4 Molecular dynamics simulation for material phase change problems

In order to understand the mechanism of phase change at a molecule resolution, MD simulations are usually conducted. They can provide important information about melting or solidification of material at the atomistic level. MD is one of numerical simulations in which atoms and molecules are allowed to interact with each other for a period of time by approximation of known physics, giving a view of the motion of the atoms/molecules. Beginning in the theoretical physics, MD method gains popularity in materials science. It is used to examine the dynamics of atomic level phenomena that cannot be observed directly, such as atoms nucleation and thin film growth. It is also a powerful tool to be used to examine the physical properties of nanomaterials that have not or cannot yet be created.

However, due to current computer resources, the size of MD simulation system cannot be too large. The computation time of a MD simulation depends on the size of system and the total time interval simulated. It may take several days even months to perform a single MD simulation. In addition, MD simulations with a long time are mathematically ill-conditioned, generating cumulative errors in numerical integrations. Although the error can be minimized with proper selection of algorithms and parameters, it cannot be eliminated thoroughly. Furthermore, most current potential functions are empirical and not sufficiently accurate to reproduce the dynamics of molecular systems in many cases.

At the early stage of computer simulation of materials [36, 37], researchers mainly focused on observing physical phenomena at single phase, i.e. liquid, solid or gas. The first computer simulation of liquid water was performed by Watts and Barker [38]. They used the Monte Carlo method to calculate water structure and properties at room temperature. The simulation of ice was first conducted by Rahman and Stillinger [39, 40]. They computed the dipole correlations and Kirkwood correlation factor of ice 1c and ice

1h.Holender [41] used Finnis-Sinclair many-body potential to study the properties of solid and liquid copper. With the development of MD theory and computer techniques, research groups employed MD simulations of water/ice to study the dynamics of the two-phase interface over the last two decades. Karim and Haymet [42-45] and other groups [46-53] did much work on simulating the interface between water and ice 1h.

For material phase change problems, Rose and Berry [54] performed MD simulation of the melting process of a KCl cluster composed of 64 ions. Alper and Politzer [55] studied the temperature-dependent behavior of aluminum, copper, and platinum by MD simulations. Luo et al. [56] performed MD simulations to investigate nonequilibrium melting and crystallization of the Lennard-Jones system, and evaluated several interfacial kinematic parameters. These simulations enhanced studies of the mechanism of phase change at the nanoscale via investigating the motion of individual atoms.

CHAPTER 3

METHODOLOGIES

3.1 Molecular dynamics

MD can be viewed as a bridge between atomic length and time scales and the micro-/macro-scopic world. It serves as an advanced method to understand the properties of systems of molecules in terms of their structure and the atomic interactions between them. MD method is based on Newton's second law or the equation of motion $F = ma$, where F is the force exerted on a particle, m is its mass and a is its acceleration. By determining the acceleration of each atom in the simulation system and integrating of the equations of motion, the positions, velocities, and accelerations of the particles will be determined then. Therefore, the average values of properties of the system can be determined, such as temperature, pressure etc. This method is deterministic. In other words, once the positions and velocities of each atom are known, the state of the system can be predicted at any time in the future or the past.

Generally, Newton's equations of motion for each atom are given as following:

$$\mathbf{F_i} = m_i \ddot{\mathbf{r}}_\mathbf{i} \tag{3.1}$$

where $\mathbf{F_i}$ is the force exerted on atom i, m_i is the mass of atom i and $\ddot{\mathbf{r}}_\mathbf{i}$ is the acceleration of atom i, which is the second derivative of position of atom i with time. The force can also be expressed as the gradient of the potential energy $U(\mathbf{r})$ if there are no external forces:

$$\mathbf{F_i} = -\nabla_i U(\mathbf{r}) \tag{3.2}$$

Combining these two equations, Newton's equations of motion can then be expressed as the derivative the potential energy to the changes in position as a function of time.

$$-\nabla_i U(\mathbf{r}) = m_i \frac{d^2 \mathbf{r}_\mathbf{i}}{dt^2} \tag{3.3}$$

3.1.1 Potential functions

To elucidate physical phenomena at the nanoscale via MD simulation, the key is to employ a potential function which can describe how the atoms/molecules to interact with each other properly. Potentials are embodying a classical treatment of particle-particle interactions that can reproduce structural and conformational changes, but usually cannot reproduce chemical reactions.

The potential function is a function of the atomic positions of all the atoms in the system, and usually expressed in terms of Cartesian coordinates. It can be subdivided into two parts: internal or bonded interaction which describes the bonds, angles and bond rotations in a molecule, and external or non-bonded interaction which accounts for the force between non-bonded atoms or atoms separated by 3 or more covalent bonds.

$$U(\mathbf{r}) = E_{bonded} + E_{non-bonded} \qquad (3.4)$$

Bonded interactions are based on a fixed list of atoms. The main bonded interactions include bond stretching, bond angle, and dihedral angle interactions. A special type of dihedral interaction is used to force atoms to remain in a plane or to prevent transition to a configuration of opposite chirality. These bonded interactions are summarized in Table 3.1.
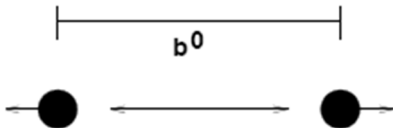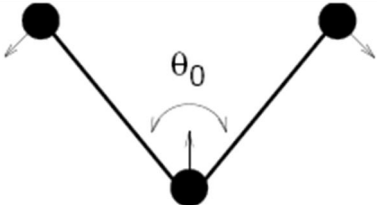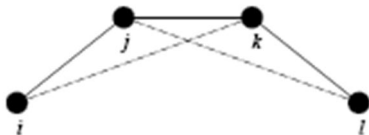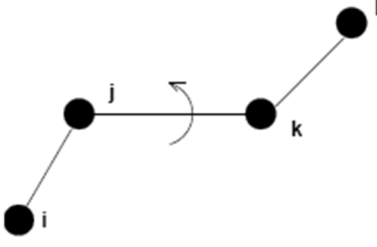
The non-bonded interaction has two components, the Van der Waals interaction and electrostatic interaction. In many simulations, simplest pair potential is often employed for Van der Waals interaction, in which the total potential energy can be calculated from the sum of energy contributions between pairs of atoms. An example of such a pair potential is 6- 12 potential (Lennard ó Jones potential):

$$E_{Van-der-waals} = \frac{C_{ij}^{12}}{r_{ij}^{12}} - \frac{C_{ij}^{6}}{r_{ij}^{6}} \qquad (3.5)$$

where the parameters C_{ij}^{12} and C_{ij}^{6} are various for different pairs of atom types. There is a potential called many body potential, in which the potential energy includes the effects of

three or more particles interacting with each other. The EAM potential is a typical many body potential, where the electron density of states in the region of an atom is calculated from a sum of contributions from surrounding atoms, and the potential energy contribution is then a function of the sum.

Table 3.1 Description of bonded interactions

Schematic Diagram	Interactions	Formulations
	Harmonic bond stretching Morse bond stretching	$E_{ij}(r_{ij}) = \dfrac{1}{2} k_{ij}^b (r_{ij} - b_{ij})^2$ $E_{ij}(r_{ij}) = D_{ij}[1 - \exp(-\beta_{ij}^b (r_{ij} - b_{ij}))]^2$
	Harmonic bond angel	$E_{ij}(\theta_{ijk}) = \dfrac{1}{2} k_{ijk}^\theta (\theta_{ijk} - \theta_{ijk}^0)^2$
	Improper Dihedrals	$E_{ij}(\phi_{ijkl}) = k_\phi (1 + \cos(n\phi - \phi_s))^2$
	Proper dihedrals	$E_{ij}(\xi_{ijkl}) = \dfrac{1}{2} k_\xi (\xi_{ijkl} - \xi_0)^2$

The electrostatic interaction between a pair of atoms is represented by Coulomb potential, and it is given by:

$$E_{electrostatic} = f \frac{q_i q_j}{\varepsilon_r r_{ij}}$$ (3.6)

where f is the constant as 138.935, and ε_r is the relative dielectric constant.

3.1.2 Integration algorithm

The potential energy is a function of the atomic positions ($3N$) of all the atoms in the system. Due to the complicated nature of this function, there is no analytical solution to the equations of motion; they must be solved numerically.

A variety of different numerical methods are developed to integrate Newton's equations of motion for updating positions of atoms from time to time. In a choosing integration method, the algorithm should conserve energy and momentum, and it should permit a long time step for integration and computationally efficient. The most often used algorithm is listed as follow:

- Leap-frog algorithm
- Verlet algorithm
- Velocity Verlet
- Predictor-corrector
- Beeman's algorithm

In my work, two of them are mainly used. The first one is Leap-frog algorithm which is most commonly used in MD simulations. Based on Taylor expansions for the positions $\mathbf{r}(t)$, the Leap-frog algorithm can be expressed as:

$$\mathbf{v}(t + \Delta t / 2) = \mathbf{v}(t - \Delta t / 2) + \mathbf{a}(t)\Delta t$$ (3.7)

$$\mathbf{r}(t + \Delta t) = \mathbf{r}(t) + \mathbf{v}(t + \Delta t / 2)\Delta t$$

In this algorithm, the velocities are first calculated at time $t + \Delta t / 2$ and then used to calculate the positions $\mathbf{r}$ at time $t + \Delta t$. Consequently, the velocities leap over the

positions, and the positions leap over the velocities. It is of third order in $\mathbf{r}$, and it is time-reversible. The advantage of this algorithm is that the velocities are explicitly calculated. However, the disadvantage is that they are not calculated at the same time as the positions.

Another integration algorithm used in my simulation is the predictor-corrector algorithm [57]. The goal is to solve the second-order differential equation:

$$\ddot{\mathbf{r}} = \mathbf{f}(\mathbf{r}, \dot{\mathbf{r}}, t) \tag{3.8}$$

where $\mathbf{f}$ is related to the forces in Newton's equation (3.1) by $\mathbf{f} = \mathbf{F}/m$, here $\mathbf{F}$ is from Equation (3.2). The first step of Predictor-corrector algorithm consists of evaluating the atoms' positions and velocities at time $t + \Delta t$ from the positions and the velocities at time $t - i\Delta t$, where i=0, 1,… … k-2, and k is being the order of the predictor part. The extrapolation for atoms positions is given by

$$\mathbf{r_i}(t + \Delta t) = \mathbf{r_i}(t) + \dot{\mathbf{r}_i}(t)\Delta t + \Delta t^2 \sum_{i=1}^{k-1} \alpha_i \mathbf{f}(t + [1-i]\Delta t) \tag{3.9}$$

and the coefficients $\{\alpha_i\}$ must satisfy the set of $k-1$ equations

$$\sum_{i=1}^{k-1} (1-i)^q \alpha_i = \frac{1}{(q+1)(q+2)}, \text{q=0,… … ,k-2} \tag{3.10}$$

These and the subsequent sets of linear equations are readily solved; the coefficients are all rational fractions. For the velocities,

$$\Delta t \dot{\mathbf{r}}_i(t + \Delta t) = \mathbf{r_i}(t + \Delta t) - \mathbf{r_i}(t) + \Delta t^2 \sum_{i=1}^{k-1} \alpha_i' \mathbf{f}(t + [1-i]\Delta t) \tag{3.11}$$

with the coefficients that satisfy equations

$$\sum_{i=1}^{k-1} (1-i)^q \alpha_i' = \frac{1}{(q+2)} \tag{3.12}$$

After computing the value of $\mathbf{f}(t + \Delta t)$ using the predicted values of $\mathbf{r_i}$ and $\dot{\mathbf{r}}_i$, the corrections are made with the aid of the Adams-Moulton formula:

$$\mathbf{r_i}(t + \Delta t) = \mathbf{r_i}(t) + \dot{\mathbf{r}}_i(t)\Delta t + \Delta t^2 \sum_{i=1}^{k-1} \beta_i \mathbf{f}(t + [2-i]\Delta t) \qquad (3.13)$$

$$\Delta t \dot{\mathbf{r}}_i(t + \Delta t) = \mathbf{r_i}(t + \Delta t) - \mathbf{r_i}(t) + \Delta t^2 \sum_{i=1}^{k-1} \beta_i' \mathbf{f}(t + [2-i]\Delta t) \qquad (3.14)$$

with the coefficients obtained from

$$\sum_{i=1}^{k-1} (2-i)^q \beta_i = \frac{1}{(q+1)(q+2)}, \quad \sum_{i=1}^{k-1} (2-i)^q \beta_i' = \frac{1}{(q+2)} \qquad (3.15)$$

It should be noted that the predicted values do not appear in the corrector formula, except for their involvement in evaluating $\mathbf{f}$. The coefficients $\{\alpha_i, \alpha_i', \beta_i, \beta_i'\}$ obtained by solving these equations for k=4 and 5 are listed in Table 3.2.

Table 3.2 Predictor-corrector coefficients for second-order equations

k=4($\times$1/24)	1	2	3	
α_i	19	-10	3	
α_i'	27	-22	7	
β_i	3	10	-1	
β_i'	7	6	-1	
k=5($\times$1/360)	1	2	3	4
α_i	323	-264	159	-38
α_i'	502	-621	396	-97
β_i	38	171	-36	7
β_i'	97	114	-39	8

The Predictor-corrector algorithm gives more accurate positions and velocities than the leapfrog algorithm, and is therefore suitable in very õdelicateö simulations. However, it is computationally expensive and needs significant storage.

3.1.3 Periodic boundary conditions

Constrained by computer resources, a finite sample is always used for MD simulations. If considering 1000 atoms arranged in a $10\times10\times10$ cubic simulation box, nearly half the atoms are on the outer faces, and these will have a large effect on the measured properties. Even for a system of 1 million atoms, the number of surface atoms still amount to 6% of the total. It is still nontrivial [57]. The classical method to minimize surface effects in a finite system is to apply periodic boundary conditions (PBC). The atoms of the system to be simulated are put into a space-filling box, which is surrounded by translated copies of itself (Fig. 3.1). Thus there are no boundaries of the system; the artifact caused by unwanted boundaries in an isolated cluster is now replaced by the artifact of periodic conditions.
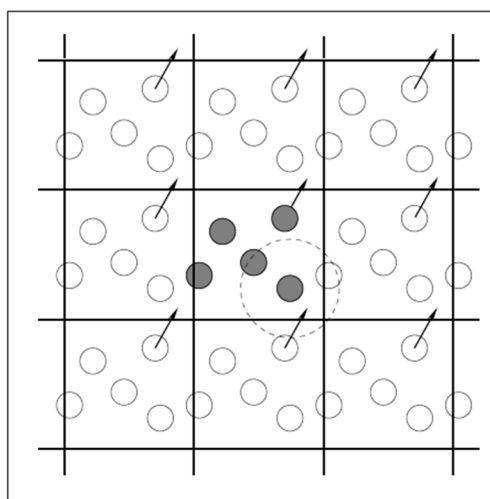
Figure 3.1 Periodic boundary conditions

Source: Michael P. Allen [57]

During MD simulation, if an atom passes through one face of the simulation box, it will reappear on the opposite face with the exactly same velocity. This is shown in Figure 3.1. Moreover, it is important to bear in mind the imposed artificial periodicity when considering properties which are influenced by long-range correlations. Special attention must be paid to the case where the potential range is not short: for example for charged and dipolar systems.

3.1.4 Temperature regulation

Several reasons such as drift during equilibration drift as a result of force truncation and integration errors, heating due to external or frictional forces, are influencing the measured properties of MD simulation. Therefore, it is necessary to control the temperature of the system. Two temperature regulation methods are used in my work. One is the weak coupling scheme of Berendsen [58], another is the extended ensemble Nose-Hoover scheme [59].

The Berendsen thermostat couples the simulation system to an external heat bath with fixed temperature T_0 to maintain the temperature of the system. The velocities are then scaled at each time step, so that the temperature deviation is proportional to the difference in temperature:

$$\frac{dT}{dt} = \frac{T_0 - T}{\tau} \tag{3.16}$$

where τ is the coupling parameter which determines how tightly the external heat bath and the system are coupled together. This method of coupling has the advantage that the strength of the coupling can be varied and adapted to the user requirement: for equilibration purposes the coupling time can be taken quite short (e.g.0.01 ps), but for reliable equilibrium runs it can be taken much longer (e.g. 0.5 ps) in which case it hardly influences the conservative dynamics.

The change in temperature between successive time steps is:

$$\Delta T = \frac{\delta t}{\tau}(T_0 - T) \tag{3.17}$$

Therefore, the time-dependent scaling factor for the velocities can be expressed as:

$$\lambda = [1 + \frac{\Delta t}{\tau_T}\{\frac{T_0}{T(t - \Delta t / 2)} - 1\}]^{1/2} \tag{3.18}$$

The $T(t - \Delta t / 2)$ in Equation (3.15) is due to the fact that the leap-frog integration algorithm is used in MD simulation. The parameter τ_T is close to, but not exactly equal to the time constant τ in Equation (3.14):

$$\tau = 2C_V \tau_{Tt} / N_{df} k \tag{3.19}$$

where C_V is the total heat capacity of the system, k is Boltzmann's constant, and N_{df} is the total number of degrees of freedom. In practice, τ is used as an empirical parameter to change the strength of the coupling. If τ is extremely large to infinite, then the Berendsen thermostat is inactive. The temperature fluctuations will grow until they reach the appropriate value of a microcanonical ensemble. On the other hand, too small values of τ will cause unrealistically low temperature fluctuations. Values of $\tau \approx 0.1 ps$ are typically used in MD simulations. The Berendsen temperature coupling is stable up to $\tau_T \approx \Delta t$.

The Berendsen temperature coupling is extremely efficient for relaxing a system to the target temperature, but once the system has reached equilibrium it might be more important to probe a correct canonical ensemble. To enable canonical ensemble simulations, the extended system method was first introduced by Nose and later modified by Hoover [59]. The system's Hamiltonian is extended by introducing a thermal reservoir and a friction term in the equations of motion. The friction force is proportional to the product of each particle's velocity and a friction parameter ξ which is a fully dynamic quantity with its own equation of motion; the time derivative is calculated from the difference between the current kinetic energy and the reference temperature.

In Hoover's formulation, the particles' equations of motion are replaced by

$$\frac{d^2\mathbf{r_i}}{dt^2} = \frac{\mathbf{F_i}}{m_i} - \xi\frac{d\mathbf{r_i}}{dt}$$

(3.20)

where the equation of motion for the heat bath parameter ξ is

$$\frac{d\xi}{dt} = \frac{1}{Q}(T - T_0)$$

(3.21)

The reference temperature is denoted T_0, while T is the current instantaneous temperature of the system. The strength of the coupling is determined by the constant Q which is usually called the 'mass parameter' of the reservoir in combination with the reference temperature. In order to avoid change Q in proportion to the change in reference temperature, it's better to directly relate Q to T_0 via:

$$Q = \frac{\tau_T^2 T_0}{4\pi^2}$$

(3.22)

This provides a much more intuitive way of selecting the Nose-Hoover coupling strength (similar to the weak coupling relaxation), and in addition τ_T is independent of system size and reference temperature.

3.1.5 Pressure coupling

Because of the same reasons as the temperature coupling, the system also needs pressure regulations. Both the Berendsen algorithm that scales coordinates and box vectors each time step, and the extended ensemble Parrinello-Rahman approach are used in my work.

The Berendsen pressure coupling rescales the coordinates and box vectors every step with a matrix , which has the effect of a first-order kinetic relaxation of the pressure towards a given reference pressure P_0

$$\frac{dP}{dt} = \frac{P_0 - P}{\tau_P}$$

(3.23)

The scaling matrix   is given by:

$$\mu_{ij} = \delta_{ij} - \frac{\Delta t}{3\tau_p} \beta_{ij} \{P_{0ij} - P_{ij}(t)\}$$ (3.24)

where β_{ij} is the isothermal compressibility of the system.

If the fluctuations in pressure or volume are important (e.g. to calculate thermodynamic properties), it might at least theoretically be a problem that the exact ensemble is not well-defined for the weak Berendsen coupling scheme. For these cases, constant-pressure simulations using the Parrinello-Rahman approach [60, 61] should be used. With the Parrinello-Rahman barostat, the box vectors as represented by the matrix b obey the matrix equation of motion:

$$\frac{db^2}{dt^2} = VW^{-1}b^{'-1}(P - P_{ref})$$ (3.25)

where V is the volume of the simulation system, W is a matrix parameter that determines the strength of the coupling. The matrices P and P_{ref} are the current and reference pressures, respectively.

The equations of motion for the particles are also changed, just as for the Nose-Hoover coupling.

$$\frac{d^2\mathbf{r_i}}{dt^2} = \frac{\mathbf{F_i}}{m_i} - M\frac{d\mathbf{r_i}}{dt}$$ (3.26)

$$M = b^{-1}[b\frac{db^{'}}{dt} + \frac{db}{dt}b^{'}]b^{'-1}$$ (3.27)

In most cases, it's better to use the combination of the Parrinello-Rahman barostat with the Nose-Hoover thermostat. In order to avoid increasing the time constant, the weak Berendsen coupling scheme is firstly used to reach the target pressure, and then switched to Parrinello-Rahman coupling once the system is in equilibrium.

3.1.6 Limitations

Classical MD represents a powerful tool in various communities including materials science. However, this method has several limitations. In fact, the atomistic systems obey the quantum law instead of a classical law. For very light systems such as H_2, H_e and N_e, the approximation via the classical MD is not good. However, MD is good for simulating heavier systems such as copper and water. This classical hypothesis can be tested through the de Brogile thermal wavelength Λ for systems consisting of atoms [62]:

$$\Lambda = (\frac{2\pi h^2}{mkT})^{1/2} \tag{3.28}$$

where h is Planck's constant , $6.62606896(33)\times10^{34} J \cdot s$, m is the mass of the atom, k is Boltzmann constant and T is the temperature. Equilibrium thermodynamics properties can be computed classically if

$$\Lambda / a << 1 \tag{3.29}$$

where a is the mean nearest neighbor distance. Since water molecules and copper atoms are much heavier than H_2, H_e and N_e, Equation (3.29) is sure enough to be satisfied.

A MD simulation requires a defined potential function. In chemistry and biology this is usually referred to a force field. Potentials may be defined at many levels of physical accuracy; those most commonly used in chemistry are based on molecular mechanics and embody a classical treatment of particle-particle interactions that can reproduce structural and conformational changes but usually cannot reproduce chemical reactions. However, current potential functions are sometimes not sufficiently accurate to reproduce the dynamics of molecular systems. Therefore the simulations are actually depending on the ability of the chosen potential to reproduce the behavior of the material under the conditions at which the simulation is run.

MD simulations update a finite sized molecular configuration forwarding in time, i.e., in a step-by-step fashion. There are limits on the typical time scale and length scale

that can be investigated and the consequences must be considered in analyzing the results. Simulation runs are typically short. Typical time step is 1femtosecond which is 1×10^{-15}s, and the typical total number of time step is around $10^{3}\sim10^{6,}$ corresponding to a few picoseconds or several nanoseconds of real time. Itøs obvious that the computation would be very expensive for long time simulation. With the development of computer resources, the number of atoms in simulation system is increasing, from hundreds to thousands and even millions. However, it will also take a long time for the simulation. Currently, it is unachievable for large system and long time simulations by the classical MD method. Because of these limitations of MD simulation, alternative methods, such as multiscale modeling methods, can be employed to study large nanoscale systems.

3.2 Temperature behaviors at the microscale

General approaches to solve phase change problems are all kind of using thermal diffusion equation to describe heat conduction during phase changing process. Within recent 30 years, some researchers found that unlike the classical theory of heat diffusion at the macroscale, the process of heat transport is governed by phonon-electron in metallic films and by phonon scattering in dielectric films from a microscopic point of view [63]. They attempted to describe the transport of energy by the microscopic energy carriers, i.e., electrons, phonons, and photons. Zhang [64] presents a state-of-the-art review of microscale heat transfer study.

3.2.1 Thermal wave model

In the past 30 years, a thermal wave model was proposed by Cattaneo (Tamma and Zhou) [65] to study heat transfer problems at the microscale. It is a modified version of Fourierøs law which is thermal diffusion equation:

$$q + \tau \frac{\partial q}{\partial t} = -k\nabla T \tag{3.30}$$

where q is the heat flux, τ is the relaxation time of the material, and k is the thermal conductivity of the material. Equation (3.30) can be combined with the transient energy equation which the internal heat source is omitted:

$$\rho c \frac{\partial T}{\partial t} + \nabla q = 0 \tag{3.31}$$

where ρ is the density of the material and c is the specific heat of the material. After combining Equation (3.30) and Equation (3.31), the following hyperbolic heat conduction equation can be obtained:

$$\tau \rho c \frac{\partial^2 q}{\partial t^2} - k\nabla^2 q + \rho c \frac{\partial q}{\partial t} = 0 \tag{3.32}$$

The governing equation in terms of temperature can be written as:

$$\tau \frac{\partial^2 T}{\partial t^2} + \frac{\partial T}{\partial t} = \alpha \nabla^2 T \tag{3.33}$$

where α is the thermal diffusivity of the material.

Li [66] compares the solutions of the thermal diffusion equation with those of the thermal wave equation for a heat transfer problem. It shows that the latter could clearly observe non-Fourier heat conduction behavior when the relaxation time of material cannot be neglected.

Through the expression of thermal wave model, it's obvious that the relaxation time τ is a very important parameter. When it is set as zero, the non-Fourier thermal wave Equation (3.33) becomes the Fourier's law thermal diffusion equation. Various expressions based on different theories have been proposed for the relaxation time for materials. If the conduction is only due to phonon transport, the relaxation time is as follows [67]:

$$\tau = \frac{3\alpha}{v^2} \tag{3.34}$$

where v is the phonon or sound velocity. For materials in which heat conduction is due to electronic transport only, the relaxation time is as follows [68]:

$$\tau = \frac{3mk}{\pi^2 nk^2 T}$$

(3.35)

where m is the effective mass, and k is Boltzmann constant here. The values of relaxation time derived from different formulation are different too. In my work, the relaxation time which is obtained from MD simulation is used in order to couple nanoscale and microscale heat transfer during phase changing process.

3.2.2 Dual-Phase-Lag model

Tzou [69] proposed a Dual-Phase-Lag model to cover the fundamental behaviors of diffusion, wave and phonon-electron interactions. In this model, two phase lags are introduced to the Fourier's law:

$$q + \tau_q \frac{\partial q}{\partial t} = -k[\nabla T + \tau_T \frac{\partial}{\partial t}(\nabla T)]$$

(3.36)

where τ_q and τ_T are the relaxation times of the material in the heat flux and the temperature gradient respectively. Equation (3.36) can be combined with the transient energy Equation (3.31), the following hyperbolic heat conduction equation can be obtained as follows:

$$\tau_q \frac{\partial^2 T}{\partial t^2} + \frac{\partial T}{\partial t} = \alpha \nabla^2 T + \alpha \tau_T \frac{\partial}{\partial t}(\nabla^2 T)$$

(3.37)

As can be seen from Equation (3.37), the Dual-Phase-Lag model converts to the Fourier's law when both the relaxation times are set to zero, and it can also convert to thermal wave model when τ_T is set to zero. Adallah [70] used this model to investigate the thermo elastic properties of a semi-infinite medium induced by a homogeneously illuminating ultra short pulsed laser heating. The results showed that the Dual-Phase-Lag model served to be more realistic to handle practically the laser problems.

<p align="center">3.3 Multiscale-based method at the microscale</p>

3.3.1 Based on thermal wave method

The thermal wave model introduced in Chapter 3.2 coupledwith MD simulation is used to investigate one dimensional ice melting problem. The flow chart is shown in Figure 3.2. FEM is used to discretize the domain including both solid and liquid regions into small uniform elements. The ice/water melting interface will locate at the grid point during the simulation. At the same time, the time step is various from time to time. In order to couple with nanoscale, I employ some of the thermal and material properties of ice and water calculated from MD simulations. The important parameter τ is also obtained from MD simulations and compared with experimental data. The detailed formulation and the method to calculate material properties are in Chapter 4.2 Microscale simulation of ice melting problem.
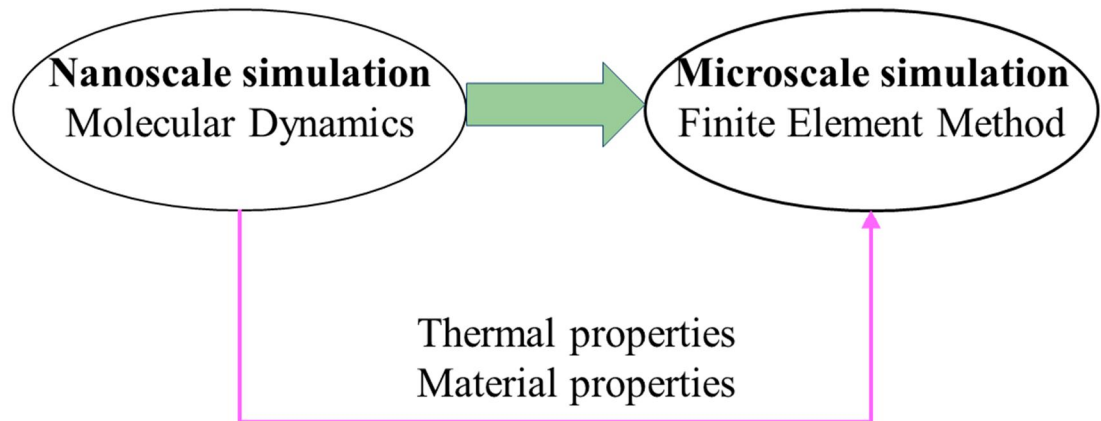
Figure 3.2 Flow chart of one-way coupling simulation for ice melting

3.3.2 Based on phase-field method

The phaseófield method coupled with MD simulation is employed to investigate copper crystallization process in microscale. The flow chart is shown in Figure 3.3.

Nuclues growth is simulated by classical phase-field method, while the interfacial parameters such as interfacial thickness, initial nucleus shape which are often assumed in current research are calculated from the MD simulations in Chapter 5.1.
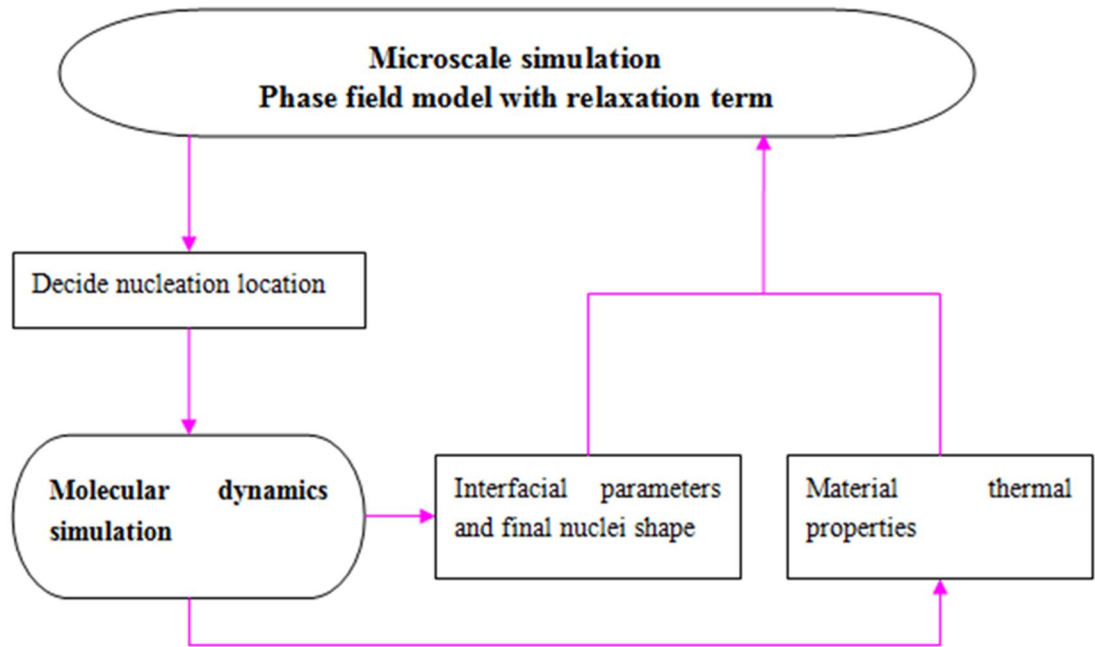
Figure 3.3 Flow chart of one-way coupling simulation for copper crystallization

The classical phaseófield model has following form:

$$\rho c_v T_t + \frac{L_f}{2} \theta_t = k \Delta T \tag{3.38}$$

$$\alpha \varepsilon^2 \theta_t = \varepsilon^2 \Delta \theta - F_\theta(\theta, T) \tag{3.39}$$

Equation (3.38) is a modified thermal diffusion equation and Equation (3.39) is the phase equation, where ε is the thickness of the solid-liquid interface, and the value is calcuated from previous Chapter by MD simulations, $F(\theta, u)$ is the free energy density function to describe the solid and liquid phases which can take on many forms, ρ is the density of the material, c_v is the specific heat, T is the temperature distribution, L_f is he

latent heat of fusion, k is the thermal conductivity, and α is the relaxation scaling. If $\theta = -1$, the material is in liquid state, and it is solid if $\theta = +1$.

Therefore, the governing equations for two dimensional phase field model are:

$$\theta_t = m\Delta\theta + \frac{m}{\varepsilon^2}\theta(1-\theta)[\theta - 0.5 + 30\varepsilon a_0 S\theta\phi(1-\theta) \tag{3.40}$$

$$\phi_t = \Delta\theta - \frac{30\theta^2(1-\theta)^2}{S}\theta_t \tag{3.41}$$

where $\phi = \dfrac{T-T_m}{T_m-T_0}, x = \dfrac{\ddot{x}}{w}, t = \dfrac{\ddot{t}}{w^2/\alpha}$.

To solve governing Equations (3.38) and (3.39), explicit scheme is employed. Let,

$$F(\theta,\phi) = \theta(1-\theta)[\theta - 0.5 + C1\theta\phi(1-\theta)] \tag{3.42}$$

$$G(\theta,\phi) = \frac{30\theta^2(1-\theta)^2}{S}\theta_t \tag{3.43}$$

After discretizating Equation (3.38) and (3.39), the following expressions can be obtained:

$$\delta\theta = m\Delta t(D_{0,x}^2 + D_{0,y}^2)\theta^n + \Delta t C_2 F(\theta^n,\phi^n) \tag{3.44}$$

$$\delta\phi = \Delta t(D_{0,x}^2 + D_{0,y}^2)\phi^n - \Delta t G(\theta^n,\phi^n) \tag{3.45}$$

where ($D_{0,x}^2 + D_{0,y}^2$) is the formal notation for a second-order central discrete Laplacian. Therefore, if θ^n and ϕ^n are known at current time step n, and boundary conditions are known too, $\theta^{n+1} = \theta^n + \delta\theta$ that is the phase field parameter at time n+1 and $\phi^{n+1} = \phi^n + \delta\phi$ which is the temperature of nodes at time n+1 can be calculated using Equation (3.44) and (3.45).

CHAPTER 4

ICE MELTING

4.1 Nanoscale simulation

4.1.1 Molecular modeling

Water is one of the most important chemical substances in nature. It is essential for the survival of living creatures. It covers 71% of the Earthøs surface and has the second-highest specific heat capacity of any known chemical compound as well as a high heat of vaporization. These two unusual properties make water play a determining role in Earthøs climate [71]. Moreover, water is very interesting in other aspects. For example, in addition to water in a liquid form, water can exist in a gas form and in 13 distinct solid crystalline forms.

Because of these unique features, a lot of research has been done to understand water properties over the last 40 years. At the early stage of computer simulation of water [72], [73], researchers mainly focused on observing physical phenomena at one phase, water liquid or ice. The first computer simulation of water was performed by Watts and Barker [74]. They used the Monte Carlo method to calculate water structure and properties at room temperature. The simulation of ice was first conducted by Rahman and Stillinger [75], [76]. They computed the dipole correlations and Kirkwood correlation factor of ice 1c and ice 1h. With the development of MD theory and computer techniques, research groups employed MD simulations of water/ice to study the dynamics of the two-phase interface over the last two decades. Karim and Haymet [77] - [80] and other [81] - [88] groups did much work on simulating the interface between water and ice 1h. These simulations mainly concerned the dynamics of ice, water, or both, or intended to obtain the melting temperature of ice. Moreover, the dynamics of ice melting, especially the melting speed, is also important to understand ice/water property.

However, there were not much work on this research especially computer simulations that could be found.

To elucidate physical phenomena at the nanoscale via MD simulation, the key issue is to choose proper potential functions. Many different potential models for water molecules have already been proposed. B. Guillot [89] summarized those models in 2002. He pointed out that SPC, SPC/E, TIP3P, TIP4P, and TIP5P were the most commonly used potential models in past years. A common criterion to choose a proper potential model is the ability to reproduce the properties of real water by computer simulations. Unfortunately, for a long time the reproduction of water properties at ambient condition (298K, 1bar) was the only concern when performing simulations by using these common potential models. However, the accuracy was not satisfying when the conditions were other than ambient. In order to reproduce thermodynamics and structural properties of water not just at ambient conditions, TIP4P-Ew, TIP4P/2005, TIP4P/ice, and TIP5P/E have been proposed and used in recent years. C. Vega [90] used these models to obtain the melting temperature with the Gibbs-Duhem methodology and obtained reasonable results.

Among the study of dynamics of ice/water interface, melting speed or crystallization speed are some of the key parameters in the phenomenon of phase change. After obtaining them, the MD simulation then can be coupled with microscale and macroscale simulation to form a whole-scale simulation of material melting or formation. The purpose of this paper in performing MD is to estimate the melting speed of ice 1h using the common potentials of SPC/E, TIP4P, TIP5P, TIP4/ice, and TIP5P/E. The reason I choose melting, not freezing, is that the latter needs a very long time for simulation via MD simulation. The difficulty lies with the fact that hydrogen bonding between individual water molecules yields a disordered three dimensional hydrogen-bond network whose rugged and complex global potential energy surface permits a large number of possible network configurations. As a result, it is very challenging to

reproduce the freezing of ÷realøwater into a solid with a unique crystalline structure. Matsumoto et al. [91] have shown the nucleation of ice from only 512 water molecules after several months of simulation within a supercomputer.

SPC/E, TIP4P, and TIP5P as well as TIP4/ice and TIP5P/E potential models are employed to conduct numerical simulations to study ice melting problem All of those potentials are in the form of the intermolecular pair potential, which has two contributions, a Lennard-Jones u_{LJ} and an electrostatic interaction u_{elec}. The expression for the potential function of water is

$$U = u_{LJ} + u_{elec} = 4\varepsilon[(\frac{\sigma}{r_{oo}})^{12} - (\frac{\sigma}{r_{oo}})^{6}] + \frac{e^2}{4\pi\varepsilon_0}\sum_{a,b}\frac{q_a q_b}{r_{ab}} \qquad (4.1)$$

where and ε are Lennard-Jones parameters, r_{oo} is the distance between the oxygen sites of two water molecules, e is the proton charge, ε_0 is the permittivity of vacuum, a and b stand for the charged sites of molecules i and j. The electrostatic interaction is between two charge sites on two water molecules. The potential parameters in Equation (4.1) for these water molecular models are listed in Table 4.1.

Table 4.1 Potential parameters of water models

Model	(Å)	ε (kJ mol-1)	qH (e)	qM (e)	ε_0
SPC/E	3.166	0.650	+0.4238	-0.8476	71
TIP4P	3.15365	0.6480	+0.5200	-1.0400	53
TIP5P	3.12000	0.6694	+0.2410	-0.2410	81.5
TIP4P/ice	3.1668	0.8822	+0.5897	-1.1794	62.9
TIP5P-E	3.097	0.7448	+0.2410	-0.2410	92

The meanings of each symbol in Table 4.1 can be found in [89] and [92].   and

are Lennard-Jones parameters. qH and qM are the charges on the hydrogen and M

sites, respectively. $_0$ is the permittivity of vacuum.

The geometry of SPC/E is the same as that of SPC, which has three interaction

sites corresponding to the three atoms of the water molecule, but the partial charges on

the H and O atoms are increased slightly in the SPC/E model. It adds an average

polarization correction to the potential energy function. Consequently, the SPC/E model

results in better density and diffusion constants than the SPC model.

In the TIP models, differences arise from the location of the negative charge. In

the TIP3P model the negative charge is located on the oxygen atom. The TIP4P model

places the negative charge on a dummy atom placed near the oxygen along the bisector of

the H-O-H angle. This improves the electrostatic distribution around the water molecule.

The first model to use this approach was the Bernal-Fowler [93] model published in

1933, which may also be the earliest water model. A new version of TIP4P is TIP4P/ice

[94]. It greatly improves the melting properties and can be used to study equilibrium

state. The TIP5P models places the negative charge on dummy atoms representing the

lone pairs of the oxygen atom, with a tetrahedral-like geometry. By reoptimizing the two

Lennard-Jones parameters of the TIP5P model, the modified version of TIP5P/E is

constructed. This model is accurate over a range of temperatures and pressures, and it

would work better than TIP5P when using Ewald sums [95].

Water has many solid phases. Being one of its crystalline phases, ice 1h

(Hexagonal ice), shown in Figure 4.1, is the form of all natural snow and ice on earth. Ice

1h crystals form hexagonal plates and columns where the top and bottom faces are basal

planes {0 0 0 1}, and the six equivalent side faces are called the prism faces {1 0 -1 0}.

Secondary prism faces {1 1 -2 0} may be formed down the planes formed by the sides of

the chair structures. Ice 1h shows anomalous reduction in thermal conductivity with

increasing pressure like ice 1c and low-density amorphous ice, but different from most

crystals. The molecular structure of ice 1h has been widely used for MD simulations by researchers to study the properties and melting temperatures of ice. In my work, ice 1h is used to conduct simulations.
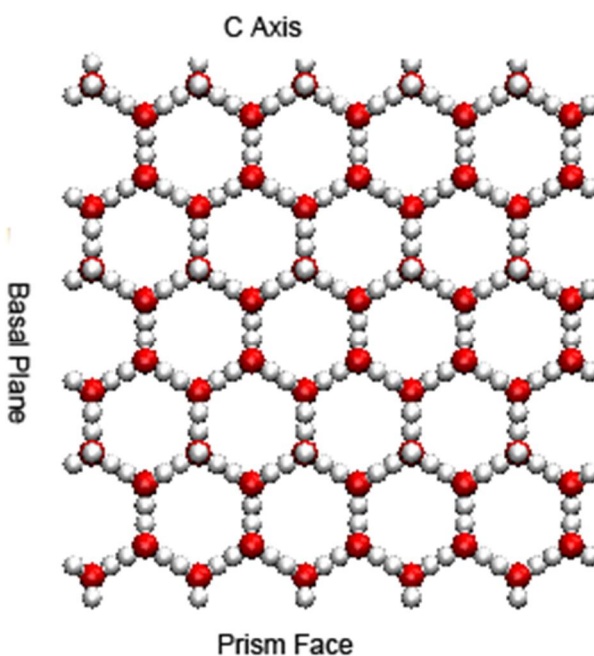
Figure 4.1 Molecular structure of ice 1h

4.1.2 Ice bulk

In this thesis, two different basic configurations are used to conduct MD simulations. The first configuration only contains ice 1h. I want to use it to simulate the melting of ice bulks. The algorithm from J. A. Hayward [96] is used to generate the ice bulk model. Periodic boundary conditions are employed on all three directions. First, run a short time MD simulation to minimize energy in order to get a proper ice structure. It is called relaxation. During relaxation, the temperature is maintained as 30K lower than the melting temperature. Then, conduct NPT MD simulations under 1 atmosphere at 30K

higher than the melting temperature [90, 96]. The time step used in simulations is 2 fs and the total simulation time is 200 ps.

I first simulate ice bulk, which contains 360 molecules and has a size of 2.24x2.33x2.19nm^3. SPC/E model is employed first. Figure 4.2 illustrates the change in the number of hydrogen bonds during the simulation. Some hydrogen bonds will be broken during ice melting. It can be clearly found that ice starting to melt around time 40 ps and totally melt around time 70 ps. Figure 4.3 shows the evolutions of the simulated bulk ice at different times: 0 ps, 40 ps, 50 ps, and 70 ps, respectively. When the ice starts melting, a slight disruption in the lattice first occurs inside the ice crystal. Such a disruption then expands along the plane, which is perpendicular to the lattice as shown in the circle area in Figure4.3 at 50ps. After that, melting occurs melting with the plane and expanding rapidly over the whole system.
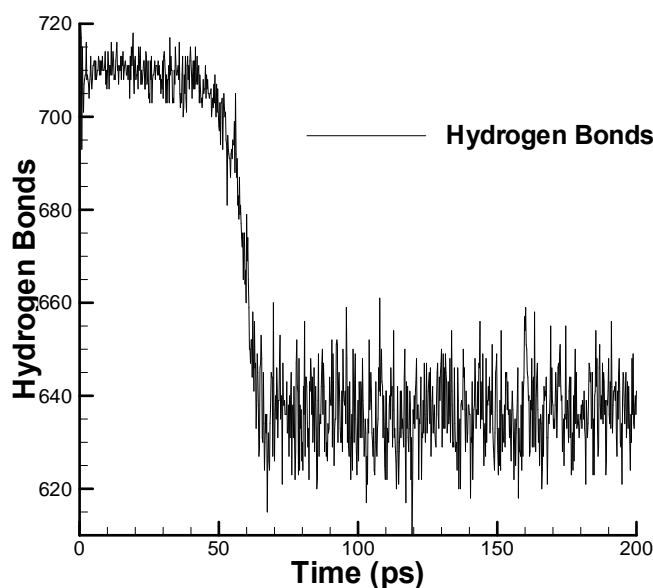
Figure 4.2 The number of hydrogen bonds with time
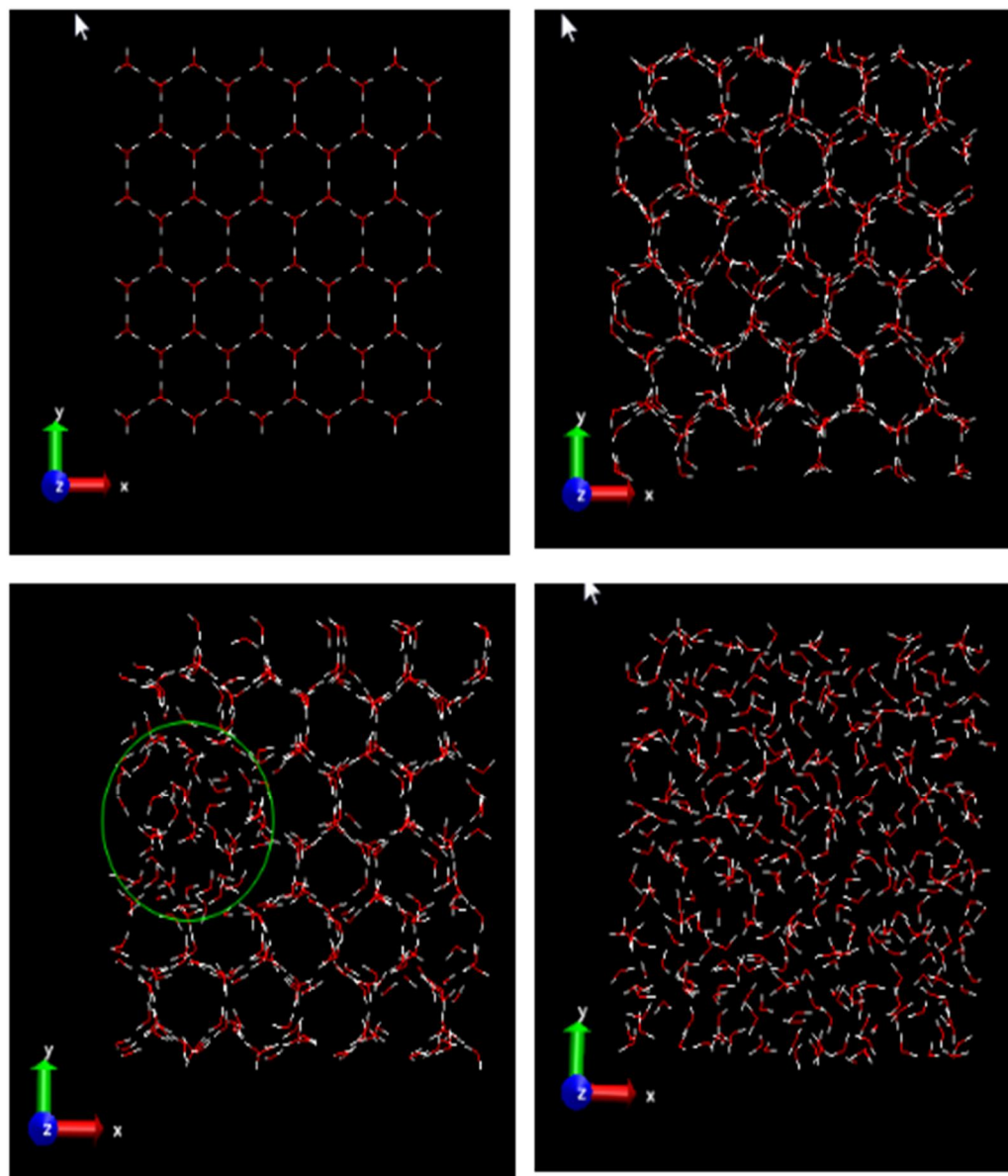
Figure 4.3 The ice crystal at different times: 0, 40, 50 and 70 ps

Table 4.2 lists the melting times of different water models. It can be found that the melting times of the simulated ice bulk for various potential models are close, except that the melting time is slightly longer if the model with higher melting temperature is employed. It should be noted that the temperature maintained in MD simulation is the melting temperature as described in Table 4.2

Table 4.2 Melting time of different water models

Model	Melting temperature (K)	Melting time (ps)
SPC/E	213	30.00
TIP4P	230	32.00
TIP4P/ice	269	34.00
TIP5P-E	271	35.00
TIP5P	273	35.00

In order to check the possible size effect, I conduct simulations with various sizes of ice bulks via expanding the simulation model in all of three dimensions. The volume of ice bulk in the previous simulation is 11.40 nm^3. Here the ice bulks with the following volumes: 22.27 nm^3, 38.48 nm^3, and 91.20 nm^3 are studied. Since various potential models result in similar melting time, only SPC/E potential is used here. During the simulations, the melting time as well as the average melting speed is calculated in the unit of nm^3 per picosecond.

Table 4.3 compares the melting times and speeds for various sizes of ice bulks. It can be seen that the melting time is longer for the ice bulk with larger size. However, the average melting speeds are not the same for ice bulks with various sizes. The larger ice bulk has a higher average melting speed. The melting speed depends on how fast these atoms absorb thermal energies from it surrounding, i.e. the external energy bath in MD simulation. For an ice bulk with a larger size, the number of atoms coupled to the external bath is larger. Therefore, more energy is absorbed into the system per unit time. It is observed that more disruptions (areas in green circle in Figure 4.4) occur at the same time in a larger size ice bulk, so the melting happens at many locations simultaneously in the crystal, and, the melting speed is higher.

Table 4.3 Melting time of different simulation boxes

ice bulksøvolumes (nm^3)	Melting time (ps)	Melting speed (nm^3/ps)
11.4	35	0.326
22.27	40	0.557
38.48	45	0.855
91.20	50	1.824
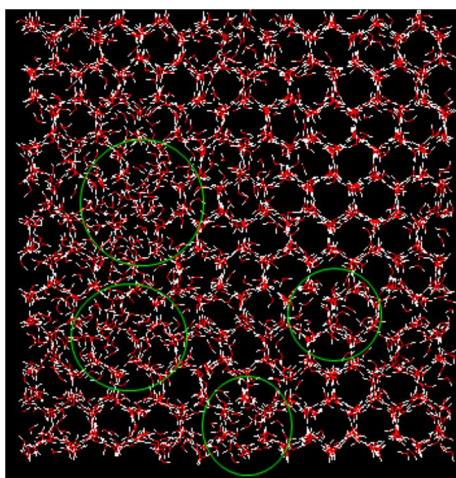
Figure 4.4 Disruptions in a large ice crystal

4.1.3 Ice/water contacting

The configuration which contains both ice and liquid water contacting with each other is then investigated. It is shown in Figure 4.5. A typical size of the simulation model is used as 67.116×23.250×21.920 Å3 with 1080 water molecules. Larger sample size up to micron meter is also available but it will cost too expensive computation time. Periodic boundary conditions are employed except the axial direction. Along the axial direction, both ends are subject to thermostats, respectively. During the simulation, the

right boundary of ice is maintained at a low temperature $T_0 = 253K$, while the left boundary of water is maintained at a high temperature $T_i = 283K$. After relaxation, the NPT MD simulations are conducted under 1 atmosphere. The time step used in the simulations was 2 fs. The typical time of the simulations is about 200 ps. The melting speed is determined by observing the movement of the ice/water interface.
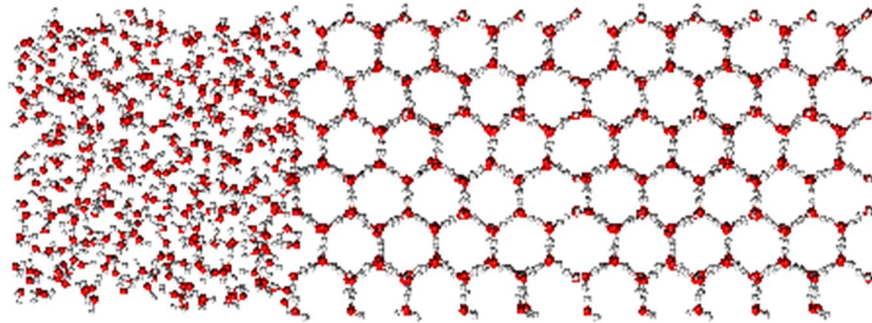

Figure 4.5 Configuration of ice/water contacting

Figure 4.6 illustrates the evolution of ice melting. When the ice starts melting, a slight disruption in the lattice first occurs inside the ice crystal but close to the interface due to absorbing heat through the interface. Such a disruption subsequently expands along a plane that is perpendicular to the lattice. Consequently, melting begins at such a plane and expands rapidly from left to right. During ice melting, the ice/water interface can be identified, although it is not a sharp one. Therefore, the ice melting speeds can be calculated at various times, as shown in Figure 4.7. It can be seen that the melting speed is very fast at the beginning and then decreases with time. Based on the discrete data obtained from the simulation, the melting speed of the ice/water interface can be predicted with the following formula,

$$v = \frac{3.7}{\sqrt{t}} e - 5 \qquad (4.2)$$
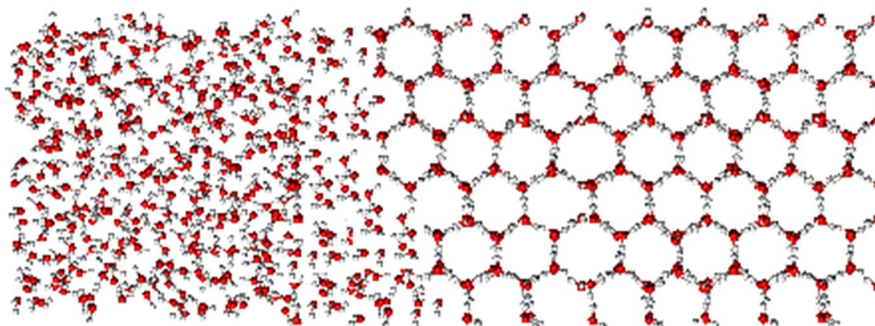
a. Interface at time 15ps
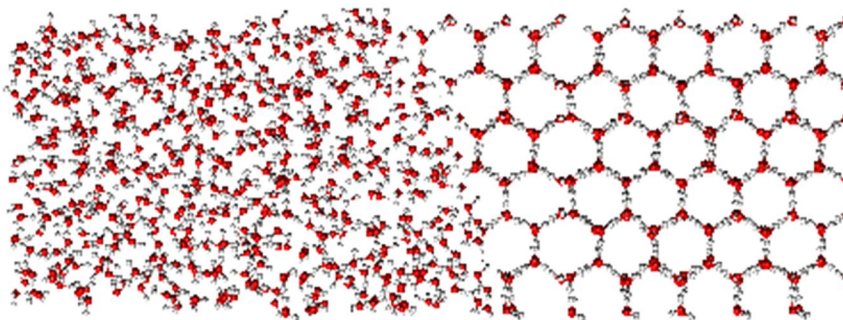
b. Interface at time 30ps
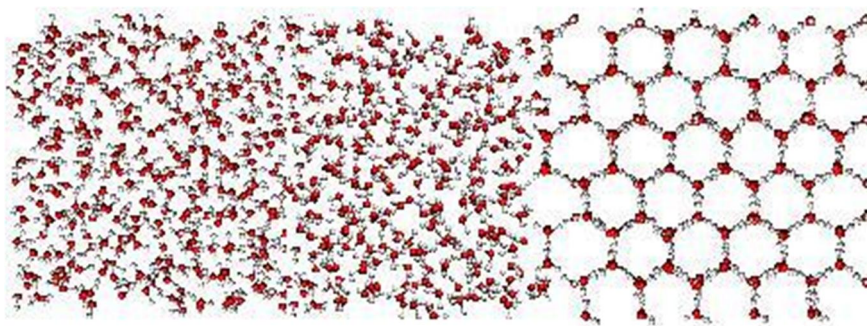
c. Interface at time 40ps

Figure 4.6 Evolution of ice/water interface
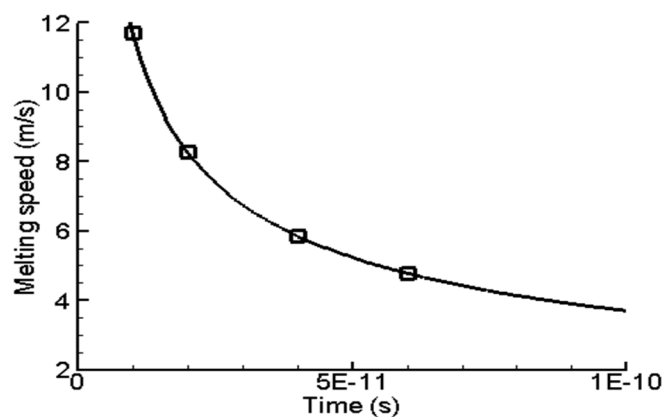
Figure 4.7 Ice melting speed

Other potential models are also employed to conduct similar MD simulation. It is found that the melting speed is independent of the potential models as shown in Figure 4.8.Figure 4.8 also shows that the melting speed decreases with time. It is because that the rate of atoms around interface absorbing energy reduces when the ice/water interface moves from one end to another end.
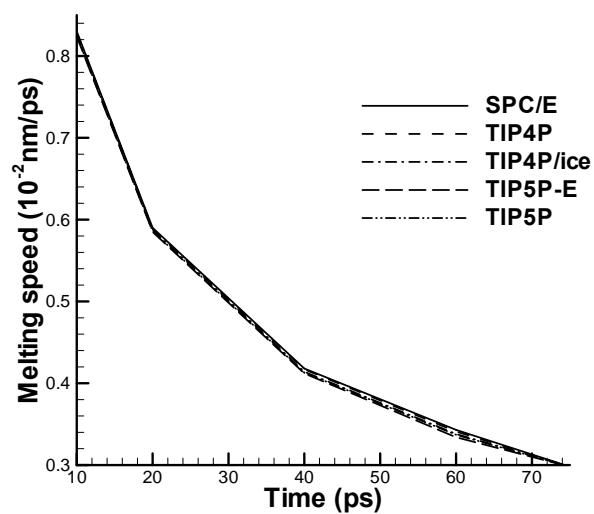
Figure 4.8 Melting speeds of different potential models

To study the size effect on the melting speed of ice/water interface, I only increase the length of the simulated model since the sides are subject to a periodic boundary condition. Because moving speeds of water/ice interface are very similar for different potentials, the TIP5P model is mainly employed here. First, keep the same temperature gradient as the previous simulation, 13.5 K per nanometer. Therefore, the temperature to which the left end of ice is subject will be decreased based on the length elongated. Figure 4.9 illustrates that there is no size effect on melting speed of ice/water interface if the temperature gradient remains the same.
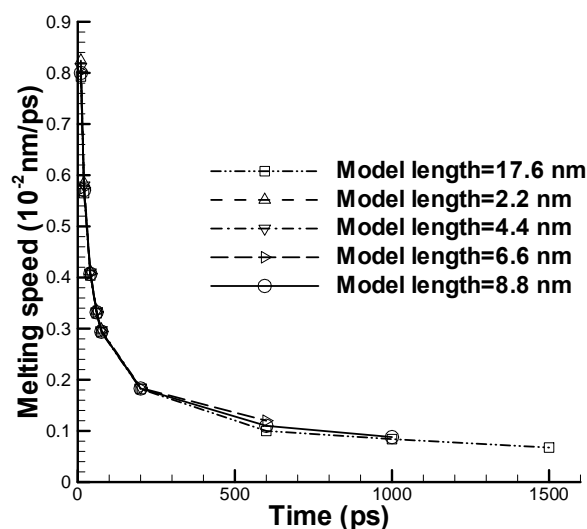
Figure 4.9 Melting speeds of different simulaiton box lengths of TIP5P

The effect of temperature gradient on the melting speed of ice/water interface is also studied. The simulated model is the same as the initial one with a length of 6.71 nm. The temperatures of the thermostats on the two ends of the simulated model are changed so that the model is subject to various temperature gradients as follows: 13.5 K, 27.0 K, 40.5 K and 54.0 K per nanometer. Figure 4.10 illustrates that the melting speed increases

as the temperature gradient increases. Obviously, high temperature gradient will accelerate the rate of atom absorbing energy. Consequently, the constant value in Equation (4.2) is related to the temperature gradient.
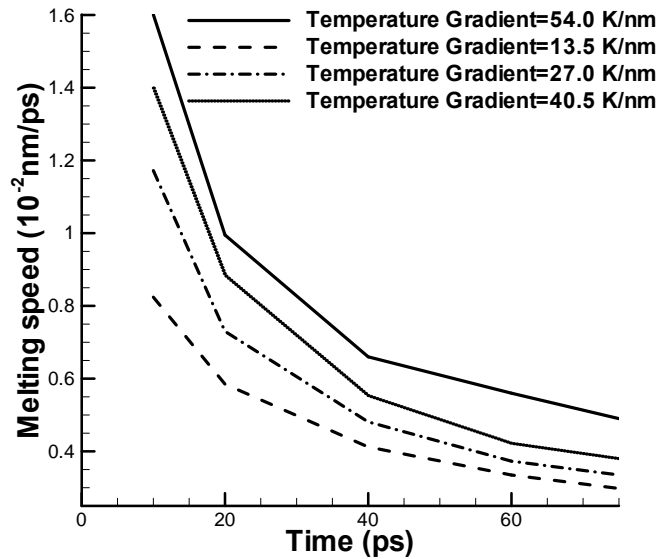
Figure 4.10 Melting speed of TIP5P with different temperature gradient

4.2 Microscale simulation

A one-dimensional ice melting problem shown in Figure 4.11 at the microscale is investigated in my work. Boundary conditions are $T(0,t) = T_i$ and $T(L,t) = T_0$, where T_i is higher than the melting temperature T_m, and T_0 is lower than T_m.

At the microscale, the melting interface is denoted as $y(t)$, which is a function of time t, and the temperature on the interface is always the melting temperature, T_m. On the melting interface, a heat transition from the solid state to the liquid state takes place. It requires a release of latent heat of transformation described via the following Equation (4.3):

$$k_s \frac{\partial T_s}{\partial x}\bigg|_{x=y(t)} - k_l \frac{\partial T_l}{\partial x}\bigg|_{x=y(t)} = \rho_s \lambda \frac{dy(t)}{dt} \tag{4.3}$$

where the subscript l refers to the liquid region, which already melted, and the subscript s refers to the solid region, which is still ice. k_s and k_l are thermal conductivities of ice and water, ρ_s is the density of ice, and λ is the latent heat of phase change.
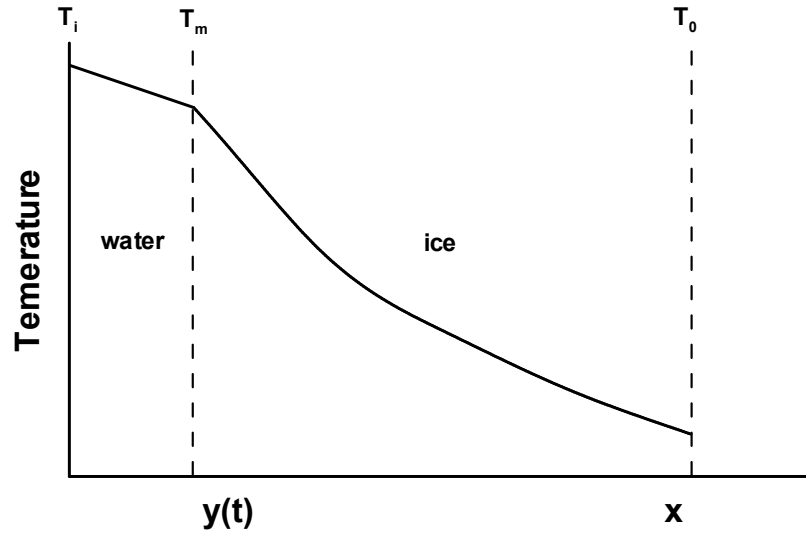
Figure 4.11 Illustration of one dimensional ice melting problem

In order to calculate the melting speed via Equation (4.3), the temperature gradients or the temperature profiles in the solid and liquid regions should be obtained. Fourier law, which is used to solve heat conduction problems at the macroscale, has been shown to be improper at the microscale. A physical-based thermal wave model (3.33) which is already explained in Chapter 3.3 is employed for the transient behavior of temperature at the microscale. In my work, only one dimension problem is considered, so Equation (3.33) has the following form:

$$\tau \frac{\partial^2 T}{\partial t^2} + \frac{\partial T}{\partial t} = \alpha \frac{\partial^2 T}{\partial x^2} \tag{4.4}$$

where τ is the relaxation time and α is the thermal diffusivity. It should be noted that the above equation will be applied on both liquid and solid regions.

For a one-dimensional ice melting problem, the entire domain, including both liquid and solid regions, is discretized into small uniform elements. The spacewise discretization of Equation (4.4), subjected to appropriate boundary conditions, can be accomplished by using the Galerkin finite element method [97]. The temperature field in one element can be approximated by nodal temperatures via the shape function N_i:

$$T^e(x,t) = \mathbf{N}^\mathbf{T}\mathbf{T}(t) = \sum_{i=1}^{n_e} N_i(x)T_i(t) \tag{4.5}$$

where $T(t)$ is the column vector of nodal temperatures, and n_e is the number of nodes per element. Two-node linear elements are used in this thesis so that n_e is equal to 2.

Substituting Equation (4.5) into the weak form of governing Equation (4.4) and integrating, the finite element equations can be written in a matrix form as:

$$\mathbf{M}\ddot{\mathbf{T}} + \mathbf{C}\dot{\mathbf{T}} - \mathbf{K}\mathbf{T} = 0 \tag{4.6}$$

and

$$M_{ij} = \tau\int N_i N_j dx, C_{ij} = \int N_i N_j dx, K_{ij} = \alpha\int (\frac{\partial N_i}{\partial x}\frac{\partial N_j}{\partial x})dx \tag{4.7}$$

In my work, uniform element length Δx is employed and the melting interface is located at the grid point during the simulation. Consequently, the time step will be various from time to time. When updating the solution from time t^n to time t^{n+1}, $\mathbf{T}^n$ and y^n are known at time t^n. In addition, at time $t^{n+1} = t^n + \Delta t^n$, $y^{n+1} = y^n + \Delta y$ is also known. It should be noted that $\Delta y = \Delta x$.

To update the solution at time t^{n+1}, the nodal temperatures $\mathbf{T}^{n+1}$ and the time step Δt^n need to be calculated. The nodal temperatures can be updated from Equation (4.6), and the time step Δt^n will be obtained from Equation (4.3) as follows

$$\Delta t^n = \frac{\rho_s \lambda}{\Delta y} \left\{ k_s [\sum_i \frac{\partial N_i (y^{n+1})}{\partial x} T_{is}^{n+1}] - k_l [\sum_j \frac{\partial N_j (y^{n+1})}{\partial x} T_{jl}^{n+1}] \right\}^{-1} \tag{4.8}$$

In my work, an iterative method is used to solve the systems of Equations (4.6) and (4.8) to obtain the nodal temperatures T^{n+1} and the time step, Δt^n, at time t^{n+1}. To start iterations at each time step, let $\Delta t^{n,0} = \Delta t^{n-1}$.The following steps are conducted in the rth (r=1, 2, 3 í) iteration to update the solution:

Step 1, substituting $\Delta t^{n,r-1}$ into Equation (4.6) to solve temperature distribution $\mathsf{T}^{n+1,r}$.

Step 2, calculating $\Delta t^{n,r}$ through Equation (4.8) by using $\mathsf{T}^{n+1,r}$ obtained from step 1.

Step 3, examining $\left| \frac{\Delta t^{n,r} - \Delta t^{n,r-1}}{\Delta t^{n,r}} \right| < \varepsilon$, where ε is the given tolerance to check if the iteration is converged. If it is converged, $\Delta t^n = \Delta t^{n,r}$ and nodal temperatures T^{n+1} are obtained at time t^{n+1}. Consequently, the ice melting speed can be calculated via $v^{n+1} = \Delta y / \Delta t^n$.

In microscale simulations, some of the thermal and material properties of ice and water are obtained from the nanoscale via MD simulations.

The thermal diffusivity α can be calculated through the thermal conductivity k divided by the product of the density and the specific heat c . The thermal conductivity k is the property of a material that indicates its ability to conduct heat [98]:

$$k = \frac{q_x}{2tA(dT / dx)} \tag{4.9}$$

where q_x is the total heat flux on x direction, dT / dx is the resultant temperature gradient in this direction, A is the surface area perpendicular to the x-axis, and t is the total simulation time. By using Equation (4.9), a thermal conductivity can be calculated from MD simulations by imposing a prescribed heat flux on the system and then

determining the resulting steady-state temperature gradient in the direction parallel to the heat flux.

The specific heat is the measure of the heat energy required to increase the temperature of the material. It can be obtained as follows [99]:

$$c = R\frac{n}{2}[1 - \frac{<K^2> - <K>^2}{\frac{n}{2}Nk_B^2T^2}]^{-1} \tag{4.10}$$

where R is the gas constant, K is the total kinetic energy of the system, n is the degree of freedom per atom, N is the total number of atoms, T is the temperature of the system, and k_B is Boltzmann constant. With MD simulations, specific heat can be calculated by a given energy fluctuation and the resulting equilibrium temperature.

Latent heat refers to the amount of energy released or absorbed by material during the phase change process. In material melting, the latent heat is equal to the difference in the enthalpy between the solid and liquid phases. The enthalpy is defined as the summation of internal energy ΔU and the product of pressure and volume change $p\Delta V$. Therefore, the latent heat λ can be calculated from MD simulation of melting of an ice bulk via

$$\lambda = \Delta U + p\Delta V \tag{4.11}$$

The relaxation time in the thermal wave equation represents the time required for the perturbed system to return into the equilibrium state. It can be calculated from a heat flux fluctuation [100]:

$$\tau = \frac{k\Delta t^2}{4L^2} \tag{4.12}$$

where k is the thermal conductivity; Δt is the real-time difference between the two peaks in the temperature response curve via MD simulations; and L is the thickness of the simulated crystal. After applying a heat flux on a given system, and measuring the time difference Δt, the relaxation time can be calculated.

4.3 Results and discussions

Material and thermal properties are calculated from MD simulations as follows:
$k_l = 0.556W/(mK)$, $\rho_l = 1000kg/m^3$, and $c_l = 4.226kJ/(kg \cdot K)$ for water;
$k_s = 2.22W/(mK)$, $\rho_s = 920kg/m^3$, and $c_s = 1.915kJ/(kg \cdot K)$ for ice. Therefore, the
thermal diffusivities are $\alpha_l = 1.32e - 7m^2/s$ and $\alpha_s = 1.26e - 6m^2/s$ for water and ice,
respectively. In addition, latent heat is calculated as $\lambda = 330kJ/kg$. Temperature effects
on those properties are neglected.

I also calculated the relaxation time of ice at various temperatures via MD
simulations. The simulated results are compared well with experimental measurements
by Petrenko and Whitworth [101] as shown in Figure 4.12. Since the relaxation time is a
function of temperature, the relaxation time I used to calculate the relaxation matrix M in
Equation (8) is corresponding to the updated temperature at each node. The calculated
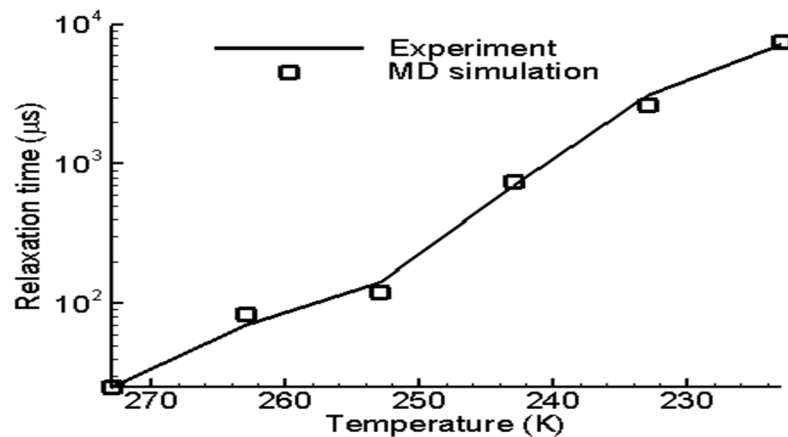relaxation time of water is very small and equals 2 ps.

Figure 4.12 Relaxation time from MD simulation compared with experimental results

By using the above material and thermal properties, the melting process of a finite
slab of ice with a thickness of $L = 10\mu m$ is analyzed. It is a typical size in microscale

simulation. The sample size up to millimeter is also available but will cost longer computation time. 1000 linear one-dimensional elements are used here. Boundary conditions are $T_i = 283K$ and $T_0 = 253K$. Based on the simulated data, the ice melting speed at the microscale can be formulated as

$$v = \frac{5.9}{\sqrt{t}} e - 5 \tag{4.13}$$

The melting speed of ice at the macroscale can be obtained from the analytical solution of an ideal one-dimensional problem [102, 103]. In this previous research, a solid at a uniform temperature T_0 that is lower than the melting temperature T_m is confined to a semi-infinite domain $x > 0$. The temperature of T_i, higher than T_m, is applied and maintained at the boundary surface, i.e., $x = 0$. As a result, the melting starts at the surface $x = 0$, and then the liquid/solid interface moves along the x direction. By solving the thermal diffusion equation and the latent heat equation, one can obtain the melting interface position as follows:

$$y(t) = 2\beta(\alpha_l t)^{1/2} \tag{4.14}$$

where β is a constant and is determined by solid and liquid temperature through:

$$\frac{e^{-\lambda^2}}{erf(\lambda)} + \frac{k_s}{k_l}(\frac{\alpha_l}{\alpha_s})^{1/2} \frac{T_m - T_0}{T_i - T_m} \frac{e^{-\lambda^2(\alpha_l/\alpha_s)}}{erfc[\lambda(\alpha_l/\alpha_s)^{1/2}]} = \frac{\beta\lambda\sqrt{\pi}}{C_{Pl}(T_i - T_m)} \tag{4.15}$$

The boundary conditions are similar to those at the micro- and nanoscales: $T_i = 283K$ and $T_0 = 253K$. Consequently, the ice melting speed at the macroscale can be derived as

$$v = \frac{13.1}{\sqrt{t}} e - 5 \tag{4.16}$$

Ice melting speeds at the macroscale, microscale, and nanoscale are compared in Figure 4.13. It should be noted that not only various length scales but also the corresponding time scales are considered. In addition, the dot lines represent the predicted ice melting speeds at the nano and micro length scales with larger time scales.

Figure 4.13 clearly shows that melting speed at the nano length/time scale is much faster than those at the microscale and macroscale. Specifically, the ice melting speed is 1.2 m/s at 1 nanosecond, while it is 5.9×10-2 m/s at 1 microsecond and 13.1×10-5 m/sat 1 second.
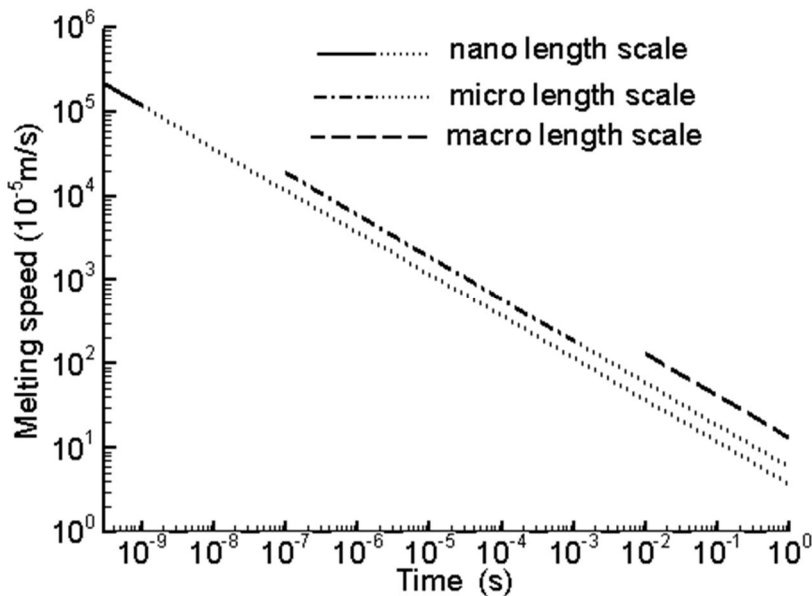
Figure 4.13 Ice melting speeds at various scales

It should also be noted that ice melting speeds decrease with time evolution as shown in Figure 4.13. If only considering various length scales, the ice melting speed at the nano length scale decreases with time. At the micro time scale, it is slower than the melting speed at the micro length scale. Similarly, at the macro time scale, the melting speeds at the micro and nano length scales are slower than the one at the macro length scale. For instance, at 1 second, the ice melting speed is 3.7×10-5 m/s at the nano length scale, 5.7×10-5 m/sat the micro length scale and 13.1×10-5 m/s at the macro length scale.

The results illustrate that the ice melting speed is scale dependent. The macroscale analytical solution is obtained based on heat transfer theory, which only describes macroscopic behaviors averaged over many grains with a long time interval. It ignores many characteristics of material at the microscale and nanoscale such as relaxation, electron-electron, and phonon-phonon scattering in material [69]. In addition, at the macroscale, the melting front is assumed to be a sharp interface, which is a mushy zone including both water and ice at the micro- or nanoscales. Consequently, ice melting at the macroscale occurs at multiple locations in the mushy zone at the micro- and nanoscales. The results of my simulations indicate that the phase change mechanism is scale dependant. In order to understand how the material phase transition, especially for nanomaterial formation, simulations and analysis in nanoscale and microscale must be conducted.

<div align="center">4.4 Conclusions</div>

In my work for ice melting, MD simulations were conducted to study melting phenomena of ice at the nanoscale. The melting of ice bulks as well as the speed of ice/water interface during ice melting was studied. Since a number of potential functions of water molecules were proposed in previous research, the following common potential functions were considered in this thesis: SPC/E, TIP4P, TIP5P, TIP4/ice, and TIP5P-E. It was found that various potential functions result in similar phenomena. Size effects were also studied on ice melting. It was found that the melting time is longer for an ice bulk with larger size but that the average melting speed is also size dependent. There is no size effect on the speed of ice/water interface during ice melting if the same temperature gradient is applied. Further research showed that such a melting speed depends on the temperature gradient.

In addition, the thermal wave model was used instead of the classical Fourier's law so that microscopic behavior of heat transfer can be accurately described in studying

ice melting at the micro length and time scale. The ice melting speeds obtained at the nano- and microscales were then compared with the analytical solution, which was derived at the macro length and time scale. It is found that ice melting speeds are different at various length and time scales. At the nano length and time scale, ice melts faster than at the micro and macro length and time scales. If only the length scale is considered, ice melts at the macroscale faster than at the nano- and microscales. It is concluded that ice melting speed is dependent not only on length scales but also on time scales. I believe that material phase change mechanisms are also scale dependent and merit further research.

CHAPTER 5

COPPER CRYSTALLIZATION

5.1 Nanoscale simulation

5.1.1 EAM potentials

The embedded-atom method (EAM) potential has been widely used in MD

simulation of metals. It was first suggested by Daw and Baskes [104,105] as a method to

overcome the main problem caused by using two-body potentials. Zheng et al [106] used

this potential to study homogeneous nucleation and growth of melting in copper. They

validated this potential using the equilibrium melting point obtained with the solid-liquid

coexistence method and the superheating-supercooling hysteresis method. Ouyang

Yifang and Zhang Bangwei et al [107,108] proposed an extended EAM potential by

adding a modified energy term to the total energy expression of the EAM. This helps to

account for the difference between the actual total energy of a system of atoms and the

one calculated from the original EAM using a linear superposition of spherically atomic

electron densities. Another modified EAM was formulated by Baskes [109,110]. It

consists of a generalization of the EAM potentials by including angular terms.

The EAM potential is used here for MD simulations of copper crystallization.

Based on the Density Functional Theory (DFT) or the Tight Binding (TB), the

following form for the total energy can be written:

$$E_{tot} = \sum_{ij}^{N} \phi_{ij}(\mathbf{r_{ij}}) + \sum_{i}^{N} F(\rho_i^h), \qquad \rho_i^h = \sum_{j} P_{ij}^{at}(\mathbf{r_{ij}}) \qquad (5.1)$$

The total energy in EAM potential consists of two parts, a pair potential term

$\phi(\mathbf{r})$ representing the electrostatic core-core repulsion, and a cohesive term $F(\rho)$

representing the energy the ion core gets when it is "embedded" in the "Electron Sea".

This embedding energy is a function of the local electron density, which in turn is

constructed as a superposition of contributions from neighboring atoms. Such an electron transfer is specified by the function $P(\mathbf{r})$.

The total energy function depends on the type of the embedded atom ($F_i(\rho)$), or on the types i and j of the two atoms involved ($P_{ij}(\mathbf{r})$, $\phi_{ij}(\mathbf{r})$). The corresponding tabulated functions can be given in either of two formats. Note that $P_{ij}(\mathbf{r})$ and $\phi_{ij}(\mathbf{r})$ have to be tabulated equidistant in r^2. The adopted tabulated EAM potential in my work was developed by Y. Mishin et al [111].

5.1.2 Central symmetry order parameter

The central symmetry order parameter is very useful for visualizing planar faults in FCC and BCC crystals [112]. Consequently, it is used to characterize the degree of inversion symmetry breaking in each atom's local environment that is to distinguish whether this atom is in solid state or liquid state. I briefly discuss the method here for how to calculate central symmetry order parameter for each atom.

An integer constant, M, is defined to be the maximum number of neighbors for the computation of the central symmetry order parameter of each atom. For an example of copper with FCC lattice structure, M is equal to 12.

For each atom $i \in 1......N$, where N is the total number of atoms

$$\tilde{m}_i \equiv \min(M, N_i) \tag{5.2}$$

$\tilde{m}_i = 0$ and the central symmetry parameter $c_i = 0$ because an isolated atom should have perfect inversion symmetry, and $\tilde{m}_i = 1, c_i = 1$ because a coordination -1 atom has no inversion image to compare with. Therefore, its inversion symmetry is the most broken. For $\tilde{m}_i \geq 2$,

$$m_i \equiv \left\lfloor \frac{\tilde{m}_i}{2} \right\rfloor \times 2 \tag{5.3}$$

With the following steps the central symmetry order parameter for each atom can be calculated:

Step 1: calculate the distance $|d_j|$ for atom i to all other atoms.

Step 2: pick up the smallest m_i, and set $|d_j|$ in ascending order. Take the smallest d_1 and the corresponding atom d_1 closest neighbor of atom i. Then search among the other $m_i - 1$ neighboring atoms of atom i to find one, i.e. atom j, which can minimize

$$\tilde{D}_j \equiv |d_1 + d_j|^2 \quad , \text{ let } j' = \arg \min_{j=2...m_i} \tilde{D}_j, D_{1 \equiv} \tilde{D}_{j'} \tag{5.4}$$

Step 3: take atoms $d1$ and j out of M atoms (here, M is 12 for copper). In remaining atoms, pick up one atom which is closest to atom i, and repeat step2 until all other atoms are empty.

Step 4: calculate the central symmetry parameter for atom i

$$c_i = \frac{\sum_{k=1}^{m_i/2} D_k}{2\sum_{j=1}^{m_i} |d_j|^2} \tag{5.5}$$

According to the Lindemann/Gilvarry rule [113], a crystal melts when the atomic vibrational amplitudes reach about ~12% of the nearest neighbor distance. Therefore, for a perfect crystal, the central symmetry parameter c_i should be less than 0.01 even at a finite temperature. In my work, the threshold value of the central symmetry parameter is set as 0.01. In other words, the atom is solid if its central symmetry parameter is less than 0.01, while the atom is liquid if its central symmetry parameter is larger than 0.01.

5.1.3 The MFPT method

The mean first passage time method (MFPT method), which was previously proposed by Wedekind [114, 115] and Bartell and Wu [116], is used to evaluate the critical nucleus size n^*, and the steady-state nucleation (barrier-crossing) rate J.

In the MFPT $\tau(x_0; a, b)$ is defined as the average elapsed time until the system beginning with state x_0 leaves a prescribed domain $[a, b]$ for the first time. In addition, the following expression can be obtained:

$$\tau(b) = \frac{\tau_J}{2}[1 + erf((b - x^*)c)] \tag{5.6}$$

where $\tau_J = 1/J$ is the inverse of the (steady-state) transition rate, and x^* represents a transition state, $c = \sqrt{\frac{|U''(x^*)|}{2kT}}$ is the local curvature at the top of the barrier, where $U(x)$ is the excess Gibbs free energy, k is the Boltzmann constant, and T is the temperature.

In the case of nucleation during crystallization, b corresponds to the size of the largest solid nucleus (n_{max}), $x^* = n^*$, and $J = 1/(\tau_J V)$, where V denotes volume, $\tau(b) = \tau(n_{max})$ can be obtained statistically from N independent runs. For each run, $n_{max}(t)$ is calculated from the trajectory via cluster analysis.

$$\tau(n_{max}) = \frac{1}{N}\sum_{i=1}^{N} t_i(n_{max}) \tag{5.7}$$

where $t_i(n_{max})$ denotes the time when the size of the largest nucleus reaches or exceeds a given value n_{max} for the first time in the ith run. Then, n*, the steady-state nucleation (barrier-crossing) rate J can be obtained by fitting to $\tau(b) = \tau(n_{max})$ with Equation (5.6).

5.1.4 Simulation details

All MD simulations for copper crystallization are conducted with a constant pressure and temperature ensemble, i.e., NPT, with three-dimensional periodic boundary conditions. Temperature is regulated with the Hoover thermostat and the isotropic pressure.

The initial configuration used for copper crystallization is shown in Figure 5.1. It only contains liquid atoms. Figure 5.1 (a) shows all the atoms, and Figure 5.1 (b) only shows the solid atoms. Such an initial configuration is obtained from melting process as shown in Figure 5.2, a perfect face-centered-cubic FCC solid copper at room temperature subjected to incremental heating, and turns into liquid regime at ambient pressure to 1800K. Then, the temperature is dropped off to the required one, i.e. 850K as shown in Figure 5.1. The temperature increment or decrement is50K.The time step employed in

MD simulations is 1 fs. At each increment/decrement temperature, the run duration includes 50 000 steps or more for the system to reach the equilibrium state. Three typical system sizes which contain 4000, 32000 and 256000 atoms are attempted to examine the size effect.
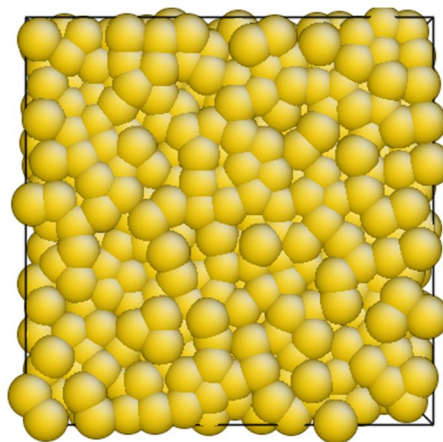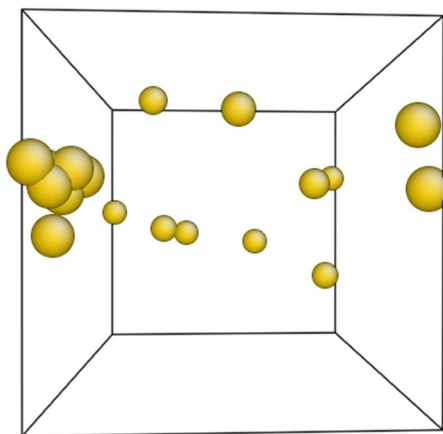

Figure 5.1 (a) Initial liquid configuration

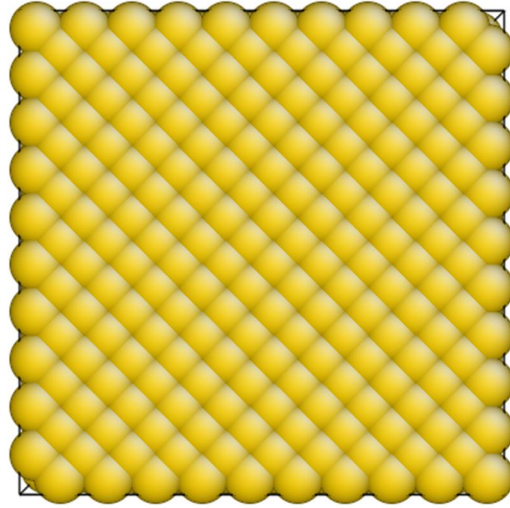Figure 5.1 (b) Initial liquid configuration (central symmetry coloring)

Figure 5.2 Initial solid configuration (4000 atoms at room temperature)

5.1.5 Atomic crystallization process: Nucleation and

Growth

In order to get homogenous crystallization, the supercooling and melting temperatures are first obtained. With 50K increment heating from room temperature 300K to 1800K and 50K decrement cooling back to 300K, the temperature and volume hysteresis is setup. Figure 5.3 shows the temperature and volume hysteresis loop for a 32000 atoms system.

T_- indicates the limit of supercooling, and T_+ indicates the limit of superheating. From Figure 5.3, $T_- = 870 \pm 10K$, $T_+ = 1620 \pm 10K$. These two values are significantly close to the supercooling and superheating temperature limits obtained by Zheng et.al. [91]. After obtaining T_- and T_+, the melting temperature of copper is easily calculated by below equation:

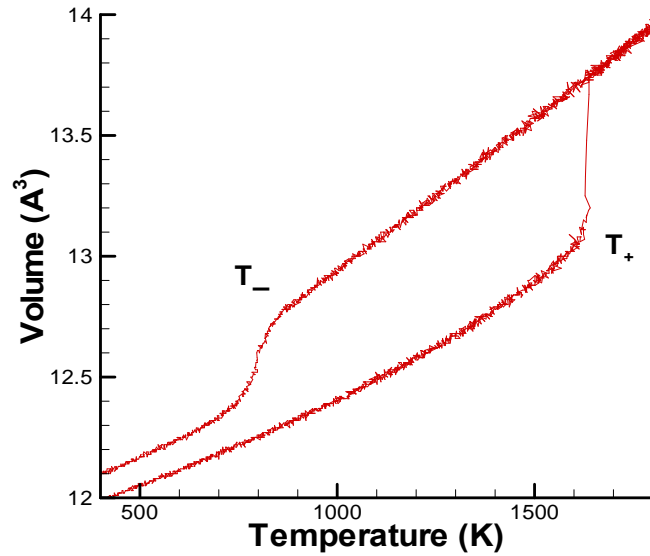$$T_m = T_- + T_+ + \sqrt{T_- T_+}$$ (5.8)

Figure 5.3 Temperature-volume hysteresis loop (32000 atoms)

Therefore, the melting temperature of copper is calculated as $T_m = 1303 \pm 20K$, which is close to the experimental data $T_m = 1358K$. In this thesis, the calculated values of supercooling and melting temperature of copper are used to do simulations.

The main purpose of MD simulation of copper crystallization is to investigate the nucleus nucleation and growth during crystallization. Therefore, the atomic coordinates are recorded every picosecond from the MD simulation for each case. Then the central symmetry parameter for each atom at a certain supercooling temperature is calculated, and solid atoms from liquid atoms are distinguished by the threshold of 0.01.

Figure 5.4 shows the evolution of copper crystallization in the case with 4000 atoms under 850K. From Figure 5.3, it can be found that crystallization starts around 20ps. At that time, a few nuclei randomly occur. However, most of them are close to the boundary. Those nuclei grow faster than others. According to the supercooling limit value $T_- = 870 \pm 10K$, it indicates that crystallization at 850K by using 850K initial configuration is heterogeneous.

Figure 5.4 Configurations of solid atoms during crystallization at 850K at 20, 30, 40 and 50ps (The system size is 4000atoms)

Figure 5.5 shows the evolution of solid atoms crystallization in the case with 4000 atoms under 900K by using initial configuration at 900K. From Figure 5.5, it can be found that crystallization starts around 2.76ns. It's very obvious that it takes much longer time to observe nucleation than the case at lower temperature, 850K in Figure 5.4. In addition, the growth rate of nuclei is also much slower than the case at the supercooling temperature of 850K. It indicates that crystallization at 900K is homogeneous, but it is hard to do simulations under this temperature because it need too much time.

Figure 5.5 Configurations of solid atoms during crystallization at 900K at 2.76, 2.77, 2.78 and 2.79 ns (The system size is 4000atoms)

The configuration with 32000 atoms is also investigated. Figure 5.6 shows the evolution of copper crystallization at850K by using initial configuration at 850K. The similar nucleation and nuclei growth to 4000 atoms at 850K is observed. The nucleation starts around 20ps and grows very fast. Nuclei randomly occur in the simulation box close to the boundary, and the nucleus which is closer to the boundary is growing faster than the nucleus which is far away from the boundary.
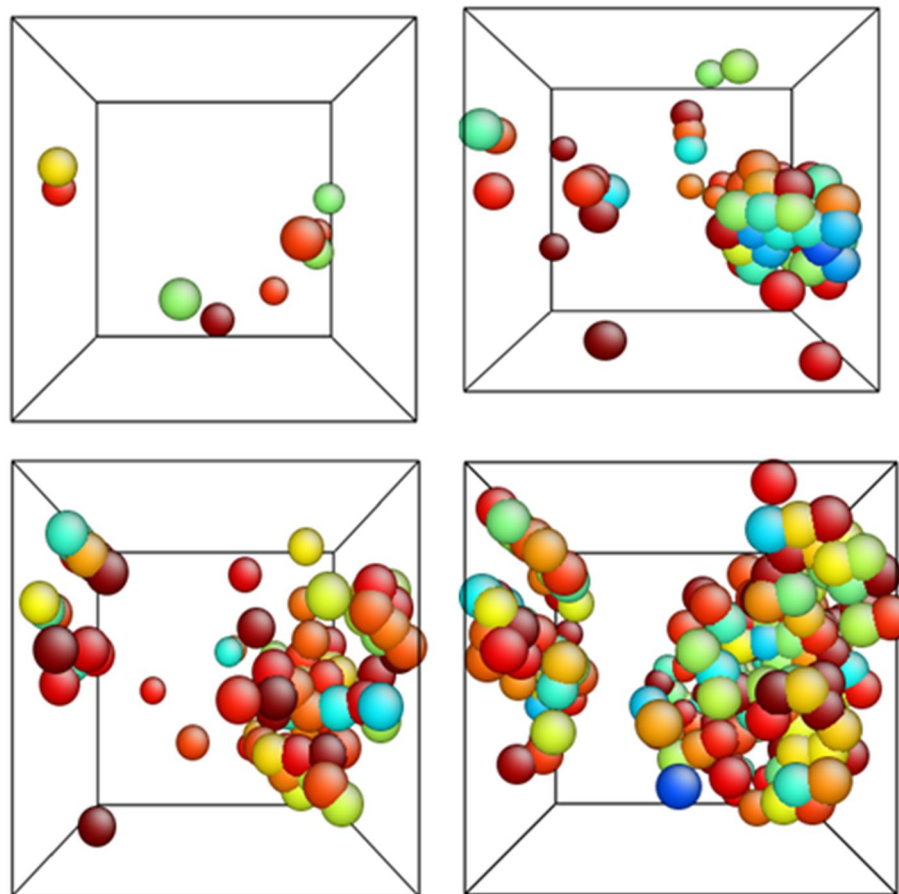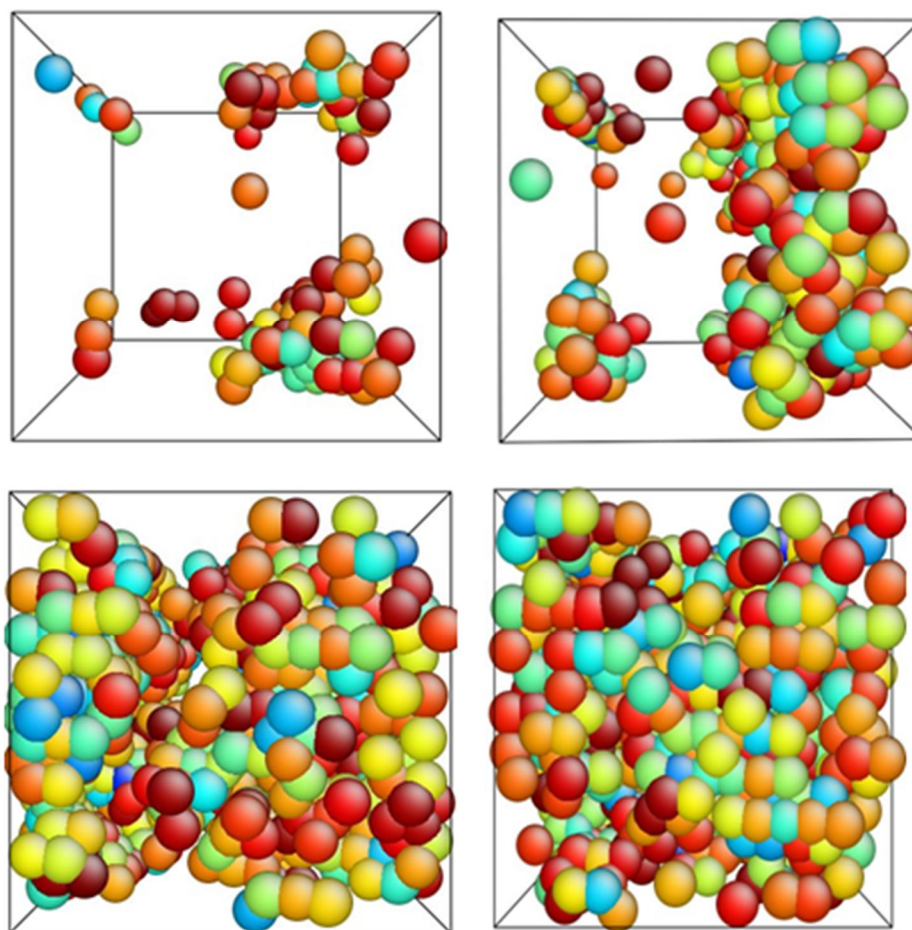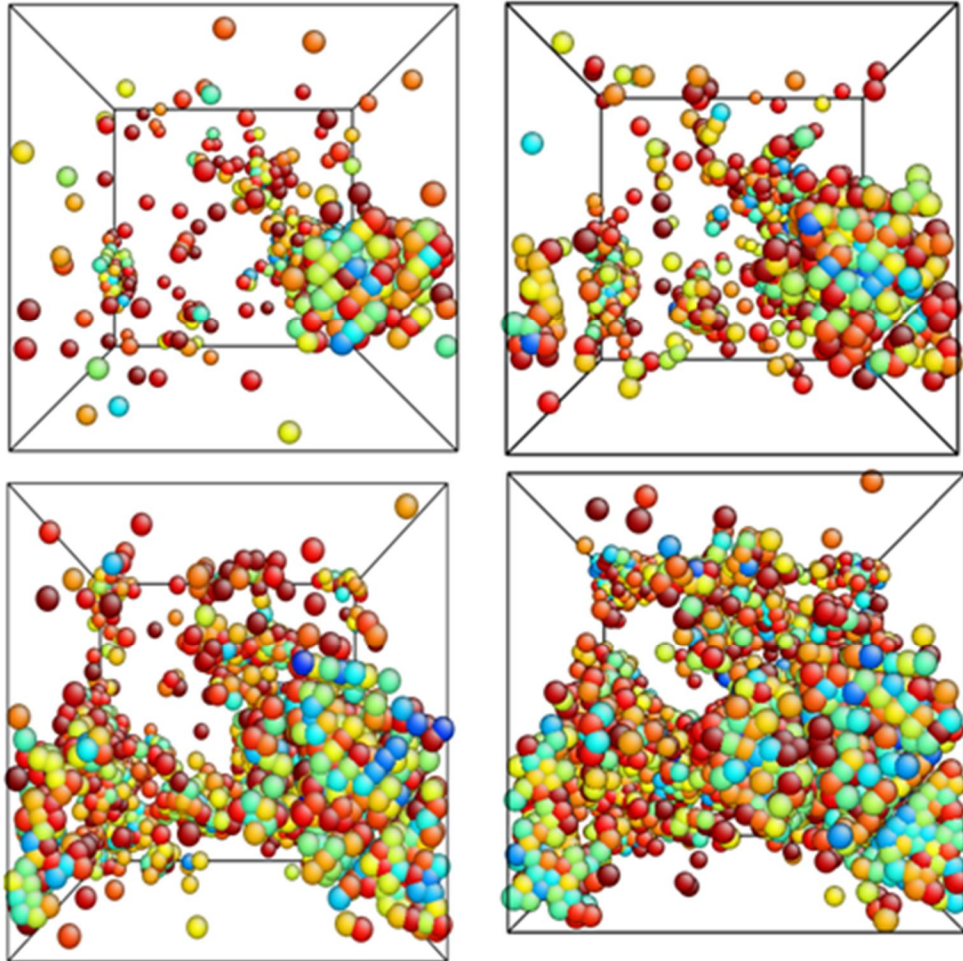
Figure 5.6 Configurations of solid atoms during crystallization at 850K at 20, 30, 40 and 50ps (The system size is 32000atoms)

The configuration with 256000 atoms is investigated to check size effect. Figure 5.7 shows the evolution of copper crystallization at850K. The similar nucleation and nuclei growth to 4000 atoms and 32000 atoms at 850K is observed too.
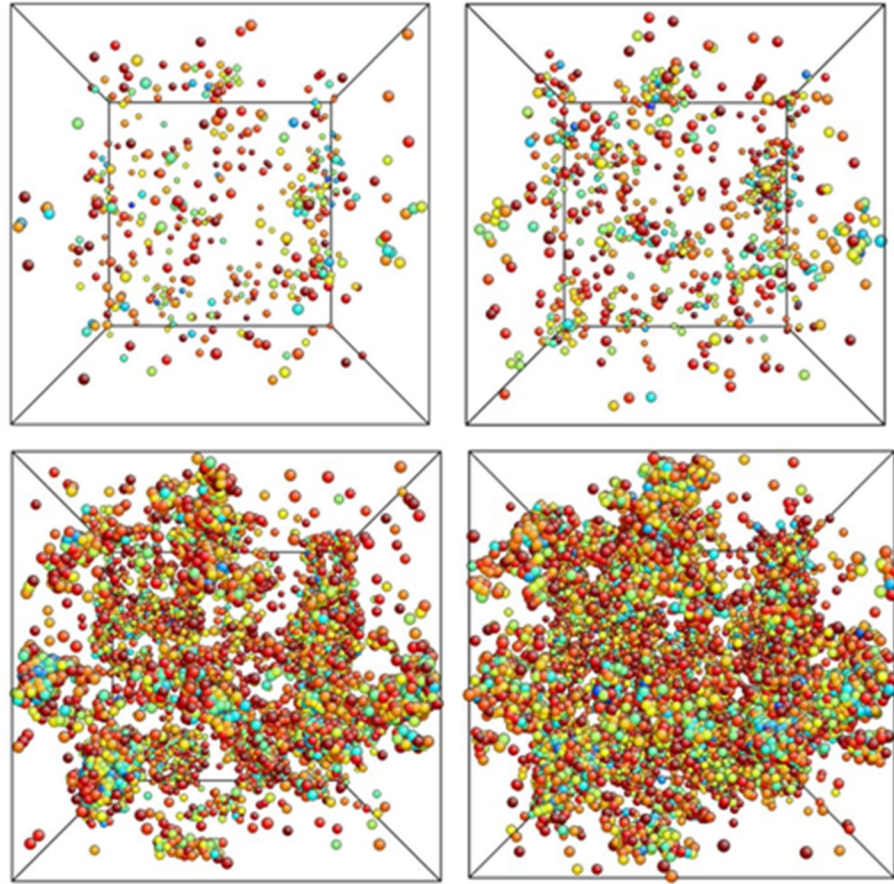
Figure 5.7 Configurations of solid atoms during crystallization at 850K at 20, 30, 40 and 50ps (The system size is 256000atoms)

Through the simulations at different temperatures, it is found that if the supercooling temperature is largely below the supercooling temperature limit 870K, heterogeneous nucleation will be observed rather than homogeneous nucleation, because no matter how the initial velocities of atoms given at the beginning, the nucleation always occur at the close area as well as close to the boundary and grows very fast. Crystallization at higher temperature, the homogeneous nucleation is observed. If different initial velocities for atoms are given, the nuclei will occur at totally different place which depends on the velocity values. Figure 5.8and Figure 5.9 show the evolution of solid atoms crystallization which has 32000 atoms under 850Kwith same initial

configuration at 875K but with different initial velocities (Random seed is used here to control initial velocity). For this case, Nucleation starts everywhere and may not be close to the boundary.
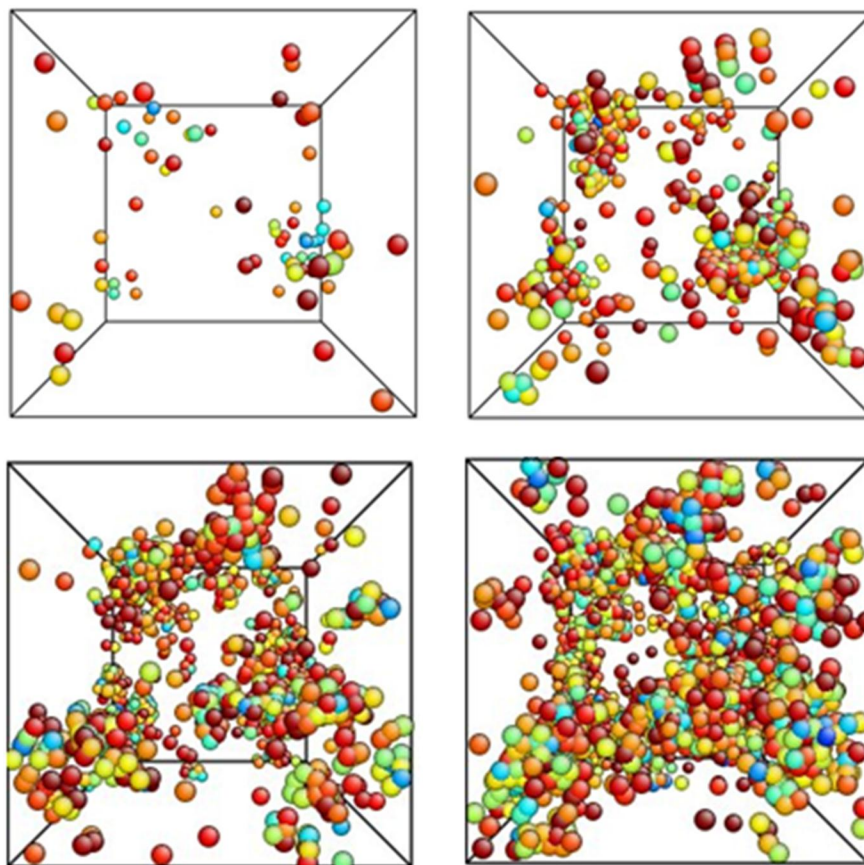
Figure 5.8 Configurations of solid atoms during crystallization at 40, 50, 60 and 70ps (The system size is 32000atoms with random seed at 99510)
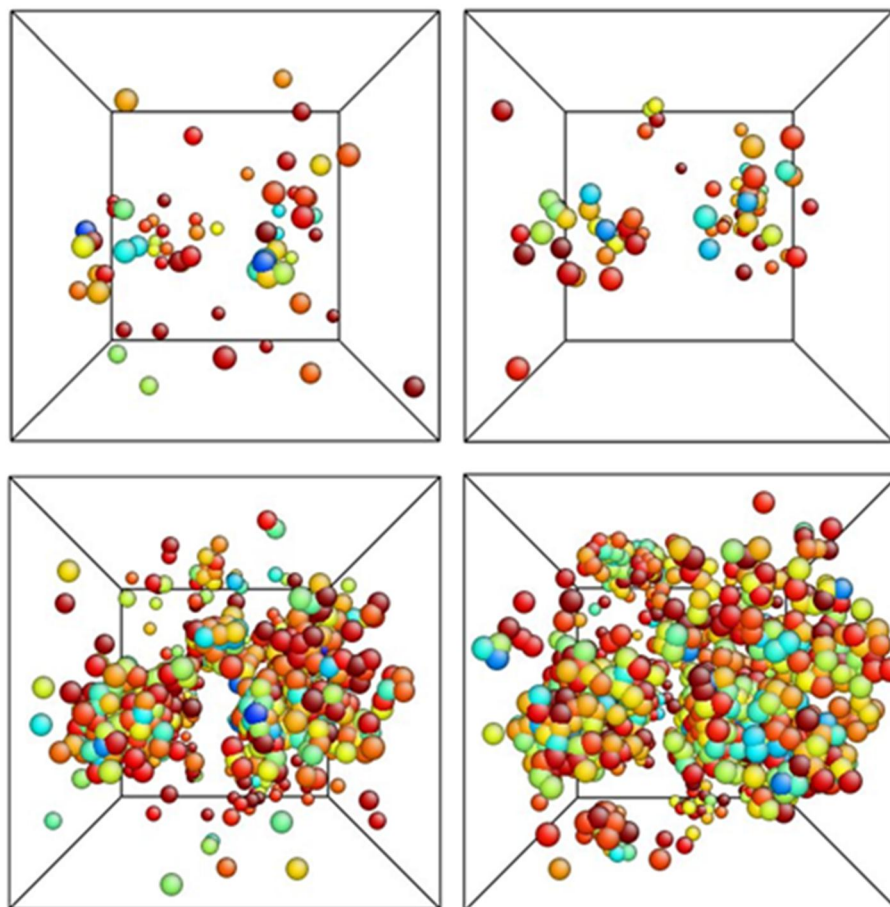
Figure 5.9 Configurations of solid atoms during crystallization at 40, 50, 60 and 70ps (The system size is 32000atoms with random seed at 493804)

Figure 5.10 shows the evolution of global central symmetry parameter as a function of time (32000 atoms crystallization under 850K by using initial configurations at 875K). Since this case is homogeneous nucleation, process of crystallization is corresponding to the configuration evolutions shown in Figure 5.7. From this graph, the crystallization process can be identified into several regimes. The first regime a is from the beginning to time around 20ps, and the second b and following regimes c, d, e and f are from time 20 to 30ps, 30 to 50ps, 50 to 100ps and thereafter respectively.
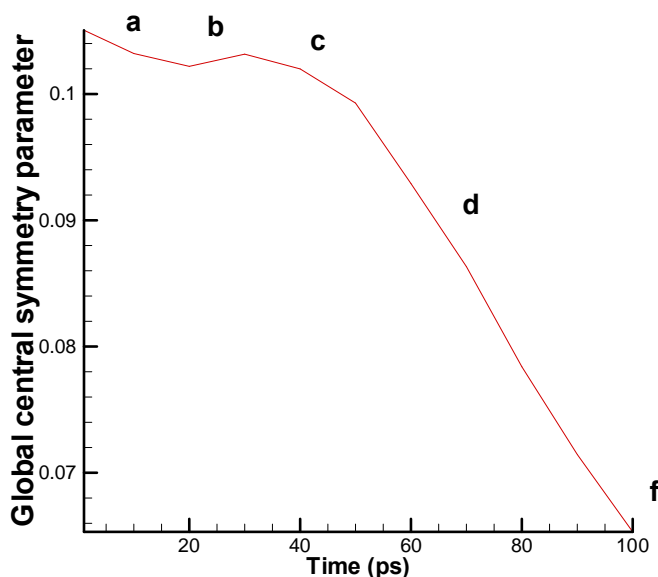
Figure 5.10 Global central symmetry parameter evolution during crystallization at 850K. The system size is 32000atoms.

The total number of solid atoms increases modestly in regime a and b, noticeably in regime c, and sharply increases in regime d. The trend to slow down is in regime f which means most atoms already become solid. In regime a, the nucleation rate is almost zero. The linear growth of the number of solid atoms occurs in regime b and c, followed by rapidly growth in regime d and then finally slows down in regime f.

In regime a, the critical nucleus has a 50% chance to transform to solid, and it also has 50% chance of reverse transition into liquid because homogeneous nucleation, which results in pronounced random fluctuation in the occurring location of the nucleus and nearly no growth in its size. In regime b, the critical nucleus is more easily transited into a super critical nucleus with more stabilized location because the possibility of its reverse transition is reduced considerably. After this period, the growth of such nucleus is stable in regime c. Fast increase in nucleation rate in both supercritical and subcritical

nucleus makes the rapid growth in regime d. The slowdown in regime f is due to depletion of parent phase, nuclei absorption, and impingement of growing supercritical nuclei.

5.1.6 Critical nucleation: the MFPT method

It is very difficult to directly obtain a rigorously defined critical nucleus with size n^* and nucleation rate J in only one individual simulation, because there is a 50% chance of reverse transition for such nuclei by definition. Therefore, the MFPT technique recently proposed by Wedekind [114] which appears appropriate for its simplicity and yet rigorousness is used. For the MFPT method, it is only necessary to consider the size of the largest nucleus n_{max}. 100 independent runs on a system of 32000 atoms at 850K are conducted. Each run starts with a different random number seed for initial velocities of atoms, but with the same initial configuration which is obtained at 850K by using the same initial configuration at 875K and all other same parameters like pressure and temperature controls. As expected, the results of all these runs are similar to each other but different in details including the location of nucleation and growth during crystallization shown in Figure 5.11.

τ is defined as the instant in the MFPT method when the size of the largest nucleus reaches or exceeds a given size n_{max} for the first time, and its value is calculated by averaging over 100runs. Fitting to with Equation (5.6), the critical nucleus is $n^* = 24$, and $J = 1/\tau_J V_{sol} = 0.8 \times 10^{38} s^{-1} m^{-3}$.
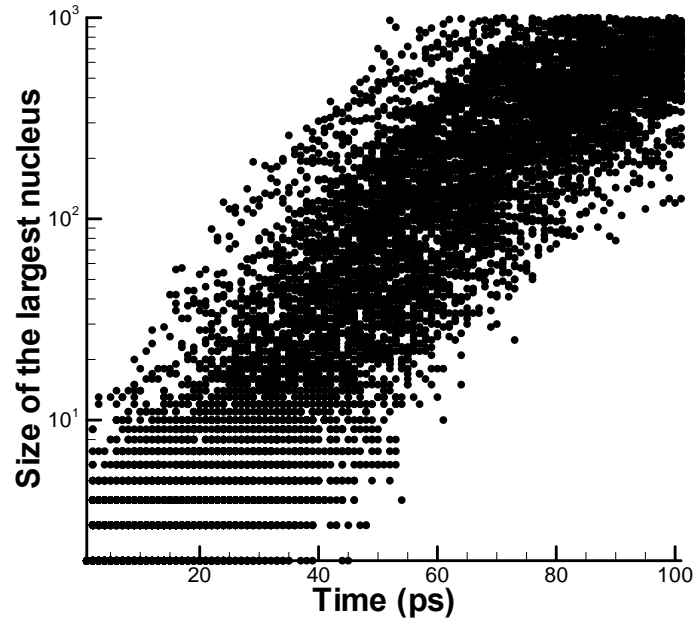
Figure 5.11 Evolutions of the size of the largest nucleus n_{max} during crystallization at 850K for a 100 independent runs with system size of 32000atoms.

5.1.7 Solid-liquid interface: thickness

Through analyzing the solid-liquid interface profile for the curved interfaces, the characteristic length scale δ (interface thickness) for the interface can be obtained.

First finding the center of mass of a certain nucleus during crystallization process, then doing spherical average centered at the center of mass (COM), i.e., starting from the COM, draw spheres of radius of r. Calculate the average central symmetry parameter within each spherical shell with a thickness of Δr, yielding a profile $c(r)$. The profile of the central symmetry parameter (denoted as c) can be described by a sigmoidal function:

$$c(r) = c_{liq} + \frac{c_{sol} - c_{liq}}{2}[1 - \tanh(\frac{r - r_0}{2w})] \tag{5.9}$$

where, r denotes the radius, r_0 is the radius of COM, and w represents a characteristic length scale of the interface. Then 10%-90% width of the interface is thus $4.394w$.

Figure 5.12 shows the cluster which contains 31 solid atoms during crystallization. It is used to calculate interface thickness here. Figure 5.13 shows the central symmetry parameter profile at the solid-liquid interface for the cluster. In this case, the solid-liquid interface between the cluster and its surrounding liquid atoms $w = 0.23nm$, and thus the corresponding interface thickness δ is 1.0nm.

Figure 5.12 A cluster with 31 atoms during crystallization at 850K
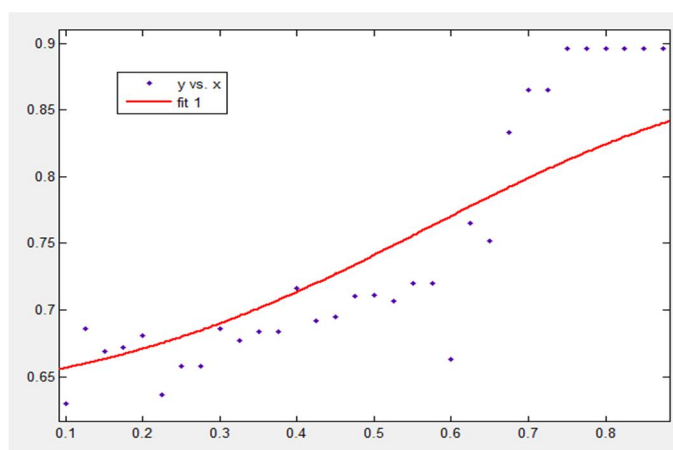
Figure 5.13 The radial central symmetry parameter profile at the solid-liquid interface of a cluster with 31 atoms

Another cluster which contains 39 solid atoms during crystallization of the system totally having 32000 atoms at 850K is also investigated, shown in Figure 5.14. Figure 5.15 shows the radial central symmetry parameter profile at the solid-liquid interface. By curve fitting, it can be found the interface thickness δ is 1.03nm which is very close to the result of 31 atoms cluster.
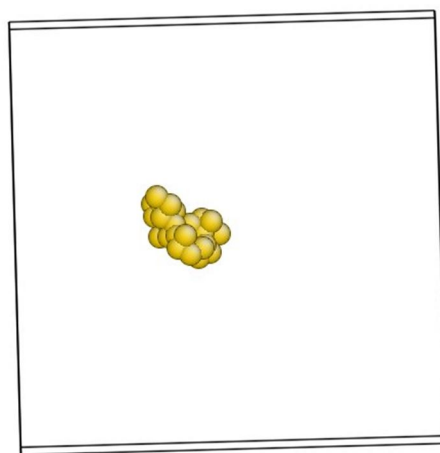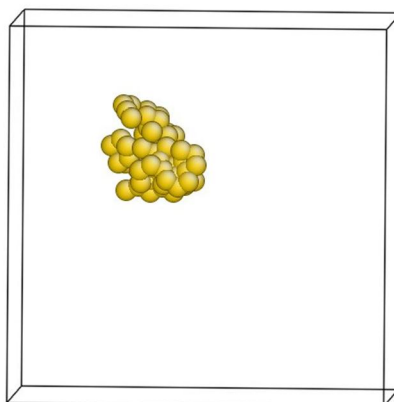

Figure 5.14 A cluster with 39 atoms during crystallization at 850K
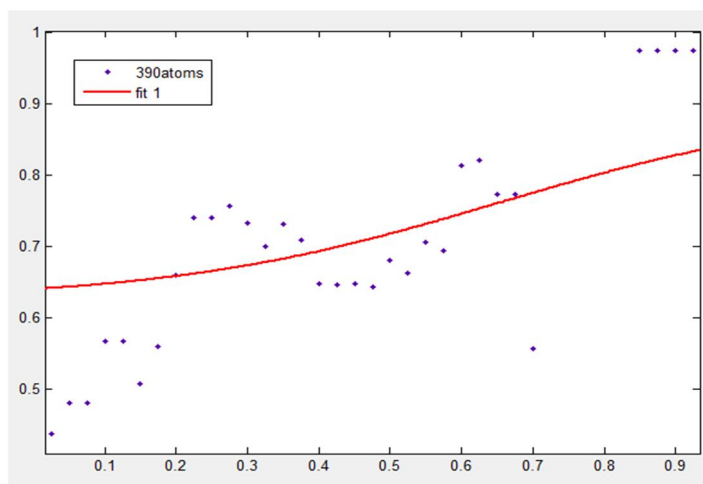
Figure 5.15 The radial central symmetry parameter profile at the solid-liquid interface of a cluster with 39 atoms

In order to check size effects, the order parameter profile of a cluster with 403 atoms in the 256000atoms crystallization process at 850K at 30ps is investigated. By curve fitting, it is found that the interface thickness δ is 1.0 nm which is very close to the result of 31 and 39 atoms clusters of system size of 32000 atoms.

5.2 Microscale simulation
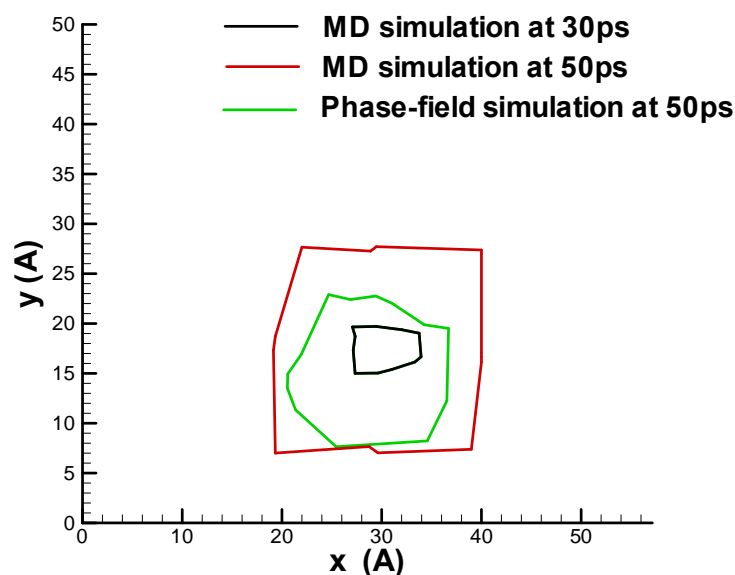
Figure 5.16 Phase-field simulation of nucleus growth comparing with MD simulation. The nuclues is chosen from a system size of 4000 atoms at 850K

The initial configuration is obtained from MD simulation of a 4000 atoms at 850K supercooling. It is the largest cluster at 30ps. Since it is a three dimensional cluster, first map it into two-dimensional configuration, and then set phase field parameter of all the nodes in this cluster to 1. It means all nodes in the initial configuration is already in solid state (The black boundary in Figure 5.16 indicates the initial configuration from

MD simulation). As shown in Figure 5.16, it can be observed that the nucleus grows

slower by phase-field method than directly MD simulation at 50ps. Since the simulation

time scale is at the nanoscale in picoseconds, it can be expected that the rough shape of

the MD nucleus will smoothens and growing into big cluster by Phase-field method. And

in contrast, MD simulation always exhibit different shapes because nucleus occur

everywhere in the simulation box, whereas the Phase-field simulation average out the

rough structures, independently of the randomly distributed initial positions of atoms.

Under non-isothermal conditions, the cluster by Phase-field method develops side

branches and evolves in a dentritic structure.
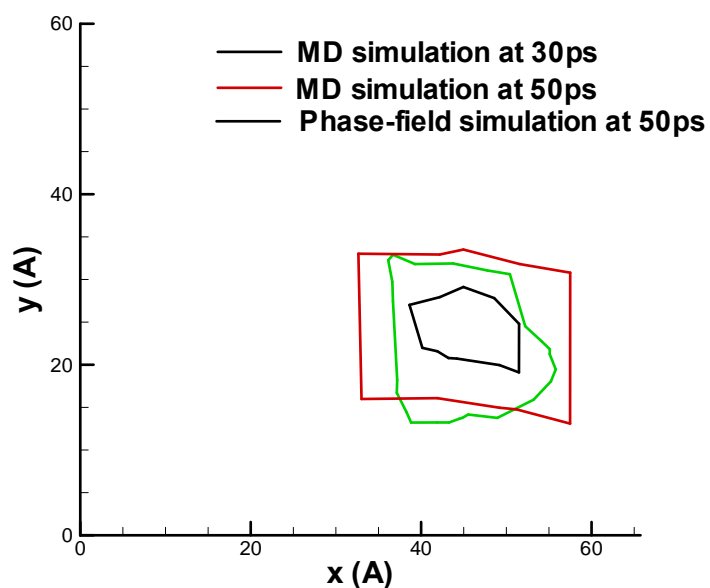
Figure 5.17 Phase-field simulation of nucleus growth comparing with MD
simulation. The nuclues is chosen from a system size of 32000 atoms at 850K

Another configuration which initial nucleus coming from the MD simulation of

system size of 32000 atoms at 850K is investigated, shown in Figure 5.17, the similar

result is observed. The phase-field method averages the roughness of the initial structure and leads into same growth in each direction of the initial nucleus at the early stage of nucleation and crystallization which is totally different from MD simulations.

5.3 Results and discussions

The Gibbs free energy difference per unit volume between solid and liquid can be calculated:

$$\Delta G_v = \Delta H_m (T - T_m)/T_m \tag{5.10}$$

where ΔH_m is the enthalpy of fusion and it equals to 12.1kJ/mol for copper.

Therefore, the excess Gibbs free energy due to the nucleation can be calculated as follow:

$$\Delta G = -\frac{4}{3}\pi r^3 \Delta G_v + 4\pi r^2 \frac{\gamma}{1 + \frac{2\delta}{r}} \tag{5.11}$$

where r is the nucleus radius, γ is the solid-liquid interfacial energy, δ is the characteristic length scale for the interface. Using the values obtained from MD simulation at 850K, $\Delta G_v = -4.188*10^3 J$, $\Delta G = 1.25*10^{-21} J$ are calculated using the assumption that $\delta = 0$ or $\delta << r$ in classical nucleation theory (CNT) [106].

In CNT, the nucleation rate can be calculated as:

$$J = J_0 * e^{-\frac{\Delta G}{kT}} \tag{5.12}$$

where J_0 is the nucleation prefactor, k is Boltzmann constant. A widely used value of J_0 for metals [117] is $10^{40} s^{-1} m^{-3}$. Using the values above, $J = 0.9*10^{40} s^{-1} m^{-3}$. It is 2 orders of magnitude larger than the nucleation rate obtained from the MFPT method. There are many debates for nucleation rate in research works [114], it may differ by 6-10 orders of magnitude depending on the methodology or assumptions adopted, and the prefactor J_0 is a main uncertainty because itsøcalculation from classical nucleation theory depends on several unknown parameters. Therefore, the MFPT method may help

to solve the controversies for copper crystallization or other materials nucleation during phase change.

The critical nucleation size is another subject under debate. From my simulations, it is about 24 atoms by MFPT method. These atoms are õstrictö solid atoms defined by central symmetry parameter in which intermediate quasi solid atoms are not accounted. While it was proposed $n^* = 12$ for simple FCC structure metals by Wang [118] based on a vacancy-squash model without considering kinetics. This value may represent a lower limit of the critical nucleation size. In classical nucleation theory, the critical nucleation size is predicted as 140 atoms when considering the finite width of the solid-liquid interface. From this aspect, one can see that the MFPT method is a rigorous technique to reduce the critical nucleation size statistically. Remember the threshold to distinguish solid and liquid atom is set to 0.01 in my simulations, the critical nucleation size may also change if changing the central symmetry threshold.

<div align="center">5.4 Conclusions</div>

In my work for copper crystallization MD simulations were conducted to study copper nucleation at the nanoscale. EAM potential was employed in simulations. The supercooling, superheating and the melting temperature were obtained. The detailed nucleation and nucleus growth at different temperatures were simulated and revealed by using central symmetry order parameter. It was found that if the supercooling temperature was largely below the supercooling temperature limit 870K, heterogeneous nucleation would be observed rather than homogeneous nucleation, the nucleation always occurred at the close area as well as close to the boundary and grows very fast. Crystallization at higher temperature, the homogeneous nucleation would be observed. If given different initial velocities for atoms, the nuclei would occur at totally different place which depends on the velocity values. 100 runs of simulations with different initial velocities were done to calculate the critical nucleus size and the steady-state nucleation

rate by the MFPT method, and compared it with the classical nucleation theory. The solid liquid interface thickness δ was calculated. For two different nuclei, the thickness values were similar about 1.0 nm. System with 4000, 32000 and 256000 atoms were examined to check size effect, and the size effect can be neglected in the early stages of nucleation during crystallization.

The Phase-field method was used to simulate copper crystallization at the microscale. The initial configuration was obtained from MD simulation of a 4000 atoms at 850K supercooling. After mapping the largest nucleus into two dimensional configuration, phase field parameter of all the nodes in this nucleus were set as 1. By phase-field method the nucleus grows slower than directly MD simulation. The reason is that phase-field simulation averages out the rough structures, independently of the randomly distributed initial positions of atoms, while MD simulation always exhibits different shapes because nucleus occur everywhere in the simulation box. And one can expect that the cluster will develop side branches and evolves in a dentritic structure by phase-field method.

CHAPTER 6

CONCLUSIONS AND FUTURE WORK

6.1 Summary and conclusions

6.1.1 Studies of ice melting

MD simulations were conducted to study ice melting at the nanoscale. Melting of ice bulks as well as the speed of ice/water interface during ice melting was studied. The common water potentials, including SPC/E, TIP4P, TIP5P, TIP4/ice, and TIP5P-E were employed. It is found that various potential functions result in similar phenomena. The size effects on ice melting were checked. It is found that the melting time is longer for an ice bulk with larger size, and the average melting speed is size dependent. There is no size effect on the speed of ice/water interface during ice melting if the same temperature gradient is applied. Further research showed that such a melting speed depends on the temperature gradient.

For ice melting at the microscale, thermal wave model instead of the classical Fourier's law was employed so that microscopic behavior of heat transfer can be accurately described in studying ice melting at the micro length and time scale. The ice melting speeds obtained at the nano- and microscales are then compared with the analytical solution, which is derived at the macro length and time scale. It is found that ice melting speeds are different at various length and time scales. At the nano length and time scale, ice melts faster than at the micro and macro length and time scales. If only the length scale is considered, ice melts at the macroscale faster than at the nano- and microscales. It is concluded that ice melting speed is dependent not only on length scales but also on time scales. I believe that material phase change mechanisms are also scale dependent and merit further research.

<u>6.1.2 Studies of copper crystallization</u>

MD simulations were conducted to study copper nucleation at the nanoscale. EAM potential was employed in simulations. System size with 4000, 32000 and 256000 atoms are investigated to check size effect.

The supercooling, superheating and the melting temperature were calculated through MD simulation, and the results had good agreement with those from literatures. The central symmetry order parameter was used to distinguish the solid and liquid atoms, and the threshold was 0.01 in my work. The detailed nucleation and nucleus growth at different temperatures were simulated and revealed. It is found that when the supercooling temperature was largely below the supercooling temperature limit of870K, heterogeneous nucleation would be observed rather than homogeneous nucleation. The nucleation always occurred at the close area as well as close to the boundary and grew very fast. The homogeneous nucleation was observed when the crystallization was at higher temperature. With different initial velocities but same initial configurations, the nuclei would occur at totally different place depending on the velocity values. The MFPT method was used to statistically calculate the critical nucleus size and the steady-state nucleation rate. Compare with the classical nucleation theory, the critical nucleation size was smaller and the nucleation rate was 2 orders of magnitude smaller. The solid liquid interface thickness δ was calculated. It was around 1.0 nm for two nuclei.

The phase-field method was used to simulate copper crystallization at the microscale. The initial configuration was obtained from MD simulation of a 4000 atoms at the supercooling temperature 850K. First mapping the largest nucleus into two dimensional configuration, then setting phase field parameter of all the nodes in this nucleus as 1, i.e., that the region was solid. It is observed that the nucleus grew slower by phase-field method than directly MD simulation. The reason is that phase-field simulation averages out the rough structures while MD simulation always exhibit different shapes because nucleus occur everywhere in the simulation box.

6.2 Recommendations for future work

In this thesis, I mainly studied phase change problems at the nanoscale and the microscale. For ice melting problem, the model used was thermal wave method. In the future work, dual phase lag method is recommended to simulate ice melting at the microscale because it has one more extra term, τ_T reflecting temperature gradient lag comparing with thermal wave method. It may be more accurate to describe phase change problem at the microscale.

For copper crystallization problem, the largest system size in MD simulations included 256000 atoms. Even I obtained good results, more large systems are highly recommended to generate better results. The issue is that a high performance computer system should be used to do such simulations. In my workstation which has 4 cores with 4G memory, a system of 256000 atoms system running 3 ns needs nearly 10 days. For microscale simulation, the modified phase-field methods using thermal wave model or dual phase lag model instead of thermal diffusion model in heat transfer equation should be interesting. From my simulation results of ice melting at the microscale, the results using thermal wave model should be more accurate.

I also recommend extending the microscale simulations from one dimension for ice melting and two dimensions for copper crystallization to three dimension simulations. The reason is obvious because three dimension simulations have perceptive results since the real world is in three dimensions no matter for ice melting or copper casting. It will not lose any information which occurred in two dimension simulations.

REFERENCES

1. Lame G; Clapeyron B P E. Memoire surla solidification par refroidissment dʹun globe solid Ann. *Chem. Phys*, 1831, 47 250ʹ60.

2. Stefan J. Uber die theorie der eisbildung, inbesondere uber die eisbildung im polarmeer Ann. *Chem. Phys*, 1891, 42 269ʹ86.

3. Neumann F. Die Paruellen Differentialgleichungen der Mathematischen Physik. 1912, vol 2 (Reimannʹ Weber) p 121.

4. Paterson S. Propagation of a boundary of fusion Proc. *Glasgow Math. Assoc*, 1952ʹ53, 1 42ʹ7.

5. Goodman T R. The heat-balance integral and its application to problems involving a change of phase Trans. *AMSE* , 1958, 80 335ʹ42.

6. Crank J. *The Mathematics of Diffusion*; Oxford: Clarendon,1975.

7. Goodman T R and Shea J J. The melting of finite slabs J. *Appl. Mech*, 1960, 27 16ʹ27.

8. Noble B. *Heat balance methods in melting problems Moving Boundary Problems in Heat Flow and Diffusion*; Oxford: Clarendon, 1975.

9. Bell G E. A refinement of heat balance integral methods applied to a melting problem. *Int. J. Heat Mass Transfer*, 1978, 21 1357ʹ61.

10. C.K.Chun and S.O.Park. A fixed-grid finite-difference method for phase-change problems. *Numerical heat transfer*, 2000, 38:59-73.

11. Boris Rubinsky. A finite element method for the solution of one-dimensional phase change problems. *Int.J. Heat transfer*, 1981

12. E. Feulvarch. An implicit fixed-grid method for the finite-element analysis of heat transfer involving phase changes. *Numerical heat transfer*, 2007, 51:585-610

13. Murray W D and Landis F. Numerical and machine solutions of transient heat-conduction problems involving melting or freezing. *J. Heat Transfer* , 1959, 81 106ʹ12.

14. Douglas J and Gallie T M. On the numerical integration of a parabolic differential equation subject to a moving boundary condition. *Duke Math. J*, 1955, 22 557ʹ71.

15. Zerroukat M and Chatwin C R. *Computational Moving Boundary Problems*; New York: Wiley, 1994.

16. Cames-Pintaux AM. Finite element enthalpy method for discrete phase change. *Numerical heat transfer*, 1986, 9:403-417

17. Tamma KK. Prediction of thermal stress and deformation due to phase change in solidifying objects via flux /stress based finite element representations. *International Journal for numerical methods in engineering*, 1994, 29:1473-1485.

18. Thevoz Ph. A general FEM code for the prediction of microstructures in castings. *The minerals, metals and materials society*, 1990, 975-984.

19. Belytschko T, MoNes N, Usui S, Parimi C. Arbitrary discontinuities in finite element. *International Journal for Numerical Methods in Engineering*, 2001, 50:993ó1013.

20. Belytschko T, Black T. Elastic crack growth in finite elements with minimal remeshing. *International Journal for Numerical Methods in Engineering*,1999, 45(5):601ó 620.

21. R. Merle and J. Dolbow. Solving thermal and phase change problems with the eXtended finite element method. *Journal of Computational Mechanics*, 2002, volume 28, number 5, pp: 339-350.

22. Jack Chessa, Patrick Smolinski, Ted Belytschko. The extended finite element method (XFEM) for solidification problems. *International Journal for Numerical Methods in Engineering*, 2002, Volume 53 Issue 8, Pages 1959 ó 1977.

23. C.L. Tien and G. Chen. Challenges in Microscale Conductive and Radiative Heat Transfer. *J. Heat Transf* , 1994, 116, 799.

24. A. Majumdar, *Microscale Energy Transport*; Taylor and Francis: London, 1998.

25. G.J. Fix. *Free Boundary Problems: Theory and Applications*, Ed. A. Fasano and M. Primicerio; Pitman, Boston, 1983, p. 580.

26. J.S. Langer. Models of pattern formation in Łrstóorder phase transitions, in *Directions in Condensed Matter Physics*, Ed. G. Grinstein and G. Mazenko, World ScientiŁc, Singapore,1986, p. 165.

27. G. Caginalp, P. Fife. Phase-field methods for interfacial boundaries. *Phys. Rev. B* , 1986, 33 (11), 7792ó7794.

28. O. Penrose, P. Fife. Thermodynamically consistent models of phase-field type for the kinetics of phase transitions. *Physica D*, 1990, 43, 44ó62.

29. S.L. Wang, R.F. Sekerka, A.A. Wheeler, B.T. Murray, S.R. Coriell, R.J. Braun, G.B. McFadden. Thermodynamically-consistent phase-field models for solidification. *Physica D*, 1993, 69, 189ó200.

30. WJ. Boettinger et a. Phase-field simulation of solidification. *Annual Review of Materials Research*, 2002, Vol. 32: 163-194.

31. Osher, S.; Sethian, J. A. Fronts propagating with curvature-dependent speed: Algorithms based on Hamilton-Jacobi formulations. *J. Comput. Phys*, 1988, 79: 12ó49.

32. Chen, S., Merriman, B., Osher, S., and Smereka, P. A simple level set method for solving Stefan problems. *Journal of Computational Physics*, 1997, 135, 8-29.

33. Kim, Y.-T., Goldenfeld, N., and Dantzig, J. Computation of dendritic microstructures using a level set method. *Phys. Rev* E., 2000, 62, 2471.

34. Lijian Tan, Nicholas Zabaras. A level set simulation of dendritic solidification with combined features of front-tracking and fixed-domain methods. *J of computational physics*, 2006, volume 211, page: 36-63.

35. Kai Wang, Anthony Changb, Laxmikant V. Kale and Jonathan A. Dantzig. Parallelization of a level set method for simulating dendritic growth. *Journal of Parallel and Distributed Computing*, 2006, volume 66, Issue 1*1*, Pages 1379-1386.

36. J. R. Reimers and R. O. Watts. A local mode potential function for the water molecule. *J. Chem. Phys.* , 1984,vol. 52, pp. 3576381.

37. J. A. Kerr and J. Kiefer. The structure, thermodynamic properties and infrared spectra of liquid water and ice. *J. Chem. Phys.*, 1988,vol. 91, pp. 2016223.

38. J. A. Barker and R. O. Watts. Structure of water; A Monte Carlo calculation. *J. Chem. Phys Letters*, 1969, vol. 3, pp.1446145.

39. Rahman, A, Stillinger. F. H, Proton Distribution in Ice and the Kirkwood Correlation Factor. *J. Chem. Phys.*, 1972, vol.57, pp. 4009 4017.

40. F. H. Stillinger. Structure of the Interface between Coexisting Fluid Phases. *Int. J. Quantum Chem,* 1982, 16, pp. 137 147.

41. Janusz M Holender. Molecular dynamics studies of solid and liquid copper using the Finnis-Sinclair many-body Potential. *J. Phys.: Condens* , 1990, Matter 2, 1291-1300.

42. J. R. Reimers and R. O. Watt. Dynamics of melting and stability of ice 1h: Molecular-dynamics simulations of the SPC/E model of water. *J. Chem. Phys.*, 2002, vol. 116, pp. 8876-8880.

43. O. A. Karim and A. D. J. Haymet. The ice/water interface. *Chem. Phys. Lett.*, 1987, vol138, pp.531-534.

44. O. A. Karim and A. D. J. Haymet. The ice/water interface: A Molecular dynamics simulation study. *J. Chem. Phys.*, 1988, vol89, pp.6889-6896.

45. . J. A. Hayward and A. D. J. Haymet. The ice/water interface: Molecular dynamics simulations of the basal, prism, {2021}, and {2110} interfaces of ice Ih. *J. Chem. Phys.*, 2001, vol114, pp.3713-3726.

46. S. W. Rick. Simulations of ice and liquid water over a range of temperatures using the fluctuating charge model. *J. Chem. Phys.*, 2001, vol114, pp.2276-2283.

47. C. Burnham, J. Li, and M. Leslie. Molecular dynamics of ice Ih using a polarizable potential. *NATO ASI Ser.*, 2000, C 561, pp.403-411.

48. S. Dong, Y. Wang, and J. Li. Potential lattice dynamical simulations of ice. *J. Chem. Phys.*, 2001, vol270, pp. 309-317.

49. J. Lekner. Energetics of hydrogen ordering in ice. *Physica B: Condensed Matter*, 1998, vol252, pp. 149-159.

50. V. Buch, P. Sandler, and J. Sadlej. Simulations of H2O Solid, Liquid, and Clusters, with an Emphasis on Ferroelectric Ordering Transition in Hexagonal Ice. *J. Chem. Phys.* , 1998, vol102, pp. 8641ó8653.

51. M. J. Vlot, J. Huinink. and J. P. van der Eerden, Free energy calculations on systems of rigid molecules: An application to the TIP4P model of H2O. *J. Chem. Phys.*, 1999, vol110, pp. 55ó61.

52. G. T. Gao and X. C. Zeng. The melting temperature of proton-disordered hexagonal ice: A computer simulation of 4-site transferable intermolecular potential model of water. *J. Chem. Phys.*, 2000, vol112, pp. 8354ó8358.

53. H. Nada and Y. Furukawa. The melting temperature of proton-disordered hexagonal ice: A computer simulation of 4-site transferable intermolecular potential model of water. *Surface Science.*, 2000, vol446, pp. 1ó16.

54. J. P. Rose and R. S. Berry. Towards elucidating the interplay of structure and dynamics in clusters: Small KCl clusters as models. *J.Chem. Phys.*, 1993, 98, 3246.

55. H. E. Alper and P. Politzer. Molecular dynamics Simulations of Neat FCC Metals Using an Alloy Potential. *J. Quantum Chem.*, 2000, 76, 670.

56. S. N. Luo, A. Strachan and D. C. Swift. Nonequilibrium melting and crystallization of a model Lennard-Jones system. *J. Chem. Phys.*, 2004, 20, 11640.

57. Michael P. Allen. Computational Soft Matter: From Synthetic Polymers to Proteins,Lecture Notes,Norbert Attig, Kurt Binder, Helmut Grubm¨uller, Kurt Kremer (Eds.),John von Neumann Institute for Computing, *J ¨ulich,NIC Series* , 2004, vol. 23, ISBN 3-00-012641-4, pp. 1-28.

58. Berendsen, H. J. C., Postma, J. P. M., DiNola. A., Haak, J. R. Molecular dynamics withcoupling to an external bath. *J. Chem. Phys.*, 1984, 81:3684ó3690.

59. Hoover, W. G. Canonical dynamics: equilibrium phase-space distributions. *Phys. Rev. A*, 1985, 31:1695ó1697.

60. Parrinello, M., Rahman. A. Polymorphic transitions in single crystals: A new Molecular dynamics method. *J. Appl. Phys.*, 1981, 52:7182ó7190.

61. Nos´e, S., Klein, M. L. Constant pressure Molecular dynamics for molecular systems. *Mol. Phys.*, 1983 50:1055ó1076.

62. J.P. Hansen and I.R. McDonald. *Theory of Simple Liquids*, 2nd ed.; Academic Press, 1986.

63. M. N. Özisik and D. Y. Tzou. On the Wave Theory in Heat Conduction. *ASME J. Heat Transf.* , 1994, 116, 526.

64. Zhuomin M. Zhang. *Nano/Microscale heat transfer*, 1ˢᵗ ed.; The McGraw-Hill company: New York, 2007.

65. Tamma, K.K. and X. Zhou. Macroscale and microscale thermal transport and thermo-mechanical interactions: some noteworthy perspectives. *J of Thermal Stresses*, 1998, 21:405-449.

66. J. Li, Z. F. Zhang and D. Y. Liu. Difference Scheme for Hyperbolic Heat Conduction Equation with Pulsed Heating Boundary. *J. Thermal Sci.*, 2000, 9(2), 152.

67. Chester, M.. Second sound in solids. *Physical review*, 1963, vol 131, pp. 2013-2016.

68. Maurer, M.J.. Relaxation model for heat conduction in metals. *Journal of Applied physics*, 1969, vol. 40, pp. 5123-5127.

69. D. Y. Tzou, Macro-to microscale heat transfer, Taylor & Francis Inc., Washington, DC, 1997

70. Ibrahim A. Abdallah. Dual phase lag heat conduction and thermal elastic properties of a semi-infinite medium induced by ultra short pulsed laser. *Progress in physics*, 2009, Vol 3.

71. American Geophysical Union. *Water Vapor in the Climate System, Special Report*. American Geophysical Union, 1995.

72. J. R. Reimers and R. O. Watts. A local mode potential function for the water molecule. *J. Chem. Phys.*, 1984, vol. 52, pp. 357ó381.

73. J. A. Kerr and J. Kiefer. The structure, thermodynamic properties and infrared spectra of liquid water and ice. *J. Chem. Phys.*, 1988, vol. 91, pp. 201ó223.

74. J. A. Barker and R. O. Watts. Structure of water; A Monte Carlo calculation. *J. Chem. Phys Letters*,1969, vol. 3,pp.144ó145.

75. Rahman, A, Stillinger, F. H. Proton Distribution in Ice and the Kirkwood Correlation Factor. *J. Chem. Phys.*, 1972, vol.57, pp. 4009 4017.

76. F. H. Stillinger. Structure of the Interface between Coexisting Fluid Phases. *Int. J. Quantum Chem*, 1982, 16, pp. 137 147.

77. J. R. Reimers and R. O. Watts. Dynamics of melting and stability of ice 1h: Molecular-dynamics simulations of the SPC/E model of water. *J. Chem. Phys.* 2002, vol. 116,pp. 8876-8880.

78. O. A. Karim and A. D. J. Haymet. The ice/water interface. *Chem. Phys. Lett.* , 1987, vol138, pp.531-534.

79. O. A. Karim and A. D. J. Haymet. The ice/water interface: A molecular dynamics simulation study. *J. Chem. Phys.*, 1988, vol89, pp.6889-6896.

80. J. A. Hayward and A. D. J. Haymet. The ice/water interface: Molecular dynamics simulations of the basal, prism, {2021}, and {2110} interfaces of ice Ih. *J. Chem. Phys.*, 2001, vol114, pp.3713-3726.

81. S. W. Rick. Simulations of ice and liquid water over a range of temperatures using the fluctuating charge model. *J. Chem. Phys.*, 2001, vol114, pp.2276-2283.

82. C. Burnham, J. Li, and M. Leslie. Molecular dynamics of ice 1h using a polarizable potential. *NATO ASI.*, 2000, Ser. C561, pp.403-411.

83. S. Dong, Y. Wang, and J. Li. Potential lattice dynamical simulations of ice. *J. Chem. Phys.*, 2001, vol270, pp. 309-317.

84. J. Lekner. Energetics of hydrogen ordering in ice. *Physica B: Condensed Matter*, 1998, vol252, pp. 149-159.

85. V. Buch, P. Sandler, and J. Sadlej. Simulations of H2O Solid, Liquid, and Clusters, with an Emphasis on Ferroelectric Ordering Transition in Hexagonal Ice. *J. Chem. Phys.*, 1998, vol102, pp. 8641ó8653.

86. M. J. Vlot, J. Huinink, and J. P. van der Eerden. Free energy calculations on systems of rigid molecules: An application to the TIP4P model of H2O. *J. Chem. Phys.*, 1999, vol110, pp. 55ó61.

87. G. T. Gao and X. C. Zeng. The melting temperature of proton-disordered hexagonal ice: A computer simulation of 4-site transferable intermolecular potential model of water. *J. Chem. Phys.*, 2000, vol112, pp. 8354ó8358.

88. H. Nada and Y. Furukawa. The melting temperature of proton-disordered hexagonal ice: A computer simulation of 4-site transferable intermolecular potential model of water. *Surface Science*, 2000, vol446, pp. 1ó16.

89. B. Guillot. A reappraisal of what we have learnt during three decades of computer simulations on water. *Journal of Molecular Liquids*, 2002, vol101, pp. 219-260.

90. Vega C, Sanz E, Abascal JL. The melting temperature of the most common models of water. *J. Chem. Phys.*, 2005, vol122, pp. 114507.

91. Masakazu Matsumoto, Shinji Saito and Iwao Ohmine. Molecular dynamics simulation of the ice nucleation and growth process leading to water freezing. *Nature*, 2002, vol416, pp.409-413.

92. S. W. Rick. A reoptimization of the five-site water potential (TIP5P) for use with Ewald sums. *J. Chem. Phys.*, 2004, vol120, pp. 6085-6093.

93. Bernal, J. D., Fowler, R.H.. A Theory of Water and Ionic Solution, with Particular Reference to Hydrogen and Hydroxyl Ions. *J. Chem. Phys.*, 1933, vol1, pp. 515.

94. J. L. F. Abascal, E. Sanz, R.G Fernández, and C. Vega. A potential model for the study of ices and amorphous water: TIP4P/Ice. *J. Chem. Phys.*, 2005, vol122, pp. 234511.

95. Ramón García Fernández, José L. F. Abascal, and Carlos Vega. The melting point of ice Ih for common water models calculated from direct coexistence of the solid-liquid interface. *J. Chem. Phys.*, 2006, vol124, pp. 144506.

96. J. A. Hayward and J. R. Reimers. Unit cells for the simulation of hexagonal ice. *J. Chem. Phys.*, 1997, vol106, pp. 1518-1529.

97. M. A. Bhatti. *Advanced topics in finite element analysis of structures with mathematica and matlab computations*; John Wiley &Sons: New York, 2006.

98. D. Bedrov and G. D. Smith. Thermal conductivity of molecular fluids from Molecular dynamics simulations: Application of a new imposed-flux method. *J. Chem. Phys.*, 2000, 113, 18.

99. P.S.Y. Cheung. On the calculation of specific heats, thermal pressure coefficients and compressibilities in molecular dynamics simulations. *Molec. Phys.*, 1977, 33 pp. 519ó526.

100. D.W. Tang and N. Araki. On non-Fourier temperature wave and thermal relaxation time. *Int. J. Thermo phys.*, 1997, 18(2), 493.

101. V. F. Petrenko and R. W. Whitworth. *Physics of Ice*; Oxford University Press: New York, 2002.

102. M. N. Özisik. *Heat conduction*; Wiley-Interscience: New Jersey, 1993.

103. W. J. Minkowycz, E. M. Sparrow, G. E. Schneider and R. H. Pletcher. *Handbook of numerical heat transfer*; Wiley-Interscience:New Jersey, 1988.

104. M. S. Daw and M. I. Baskes. Embedded-atom method: Derivation and application to impurities, surfaces, and other defects in metals. *Phys. Rev.*, 1984, B 29, 6443.

105. S. M. Foiles, M. I. Baskes, and M. S. Daw. Embedded-atom-method functions for the fcc metals Cu, Ag, Au, Ni, Pd, Pt, and their alloys. *Phys. Rev.*, 1986, B 33, 7983

106. Lianqing Zheng, Qi An and Yun Xie, Zehui Sun, Sheng-Nian Luo. Homogeneous nucleation and growth of melt in copper. *J. Chem. Physics.*, 2007, v127, 164503.

107. O. Yifang, Z. Bangwei, L. Shuzhi, and J. Zhanpeng, Z. A simple analytical EAM model for bcc metals including Cr and its application. *Phys. Chem.*, 1996, Abt. B 101, 161.

108. Z. Bangwei, O. Yifang, L. Shuzhi, and J. Zhanpeng. An analytic MEAM model for all BCC transition metals. *Physica B*, 1999, 262, 218.

109. M.I.Baskes. Modified embedded-atom potentials for cubic materials and impurities. *Phys. Rev.B*, 1992, 46, 2727.

110. M.I.Baskes. Determination of modified embedded atom method parameters for nickel. *Mater.Chem.Phys.*, 1997, 50, pp152-158.

111. Y. Mishin, M. J. Mehl, D. A. Papaconstantopoulos, A. F. Voter, and J. D. Kress. Structural stability and lattice defects in copper: Ab initio, tight-binding, and embedded-atom calculations. *Phys. Rev. B*, 2001, 63, 224106.

112. C.L. Kelchner, S.J. Plimpton, J.C. Hamilton. Dislocation nucleation and defect structure during surface indentation. *Physical Review B*, 1998, 58, 11085-8.

113. J.J. Gilvarry. The Lindemann and Gruneisen Laws. *Phys. Rev.*, 1956, 102, 308.

114. J. Wedekind, Finite-size effects in simulations of nucleation. Ph.D. thesis, University of Cologne, Cologne, 2007.

115. J. Wedekind, D. Reguera, and R. Strey. Finite-size effects in simulations of nucleation. *J. Chem. Phys.*, 2006 125, 214505.

116. L. S. Bartell and D. T. Wu. A new procedure for analyzing the nucleation kinetics of freezing in computer simulation. *J. Chem. Phys.*, 2006, 125, 194503.

117. D. A. Porter and K. E. Easterling. *Phase Transformations in Metals andAlloys*; Chapman and Hall: London, 1981

118. L. W. Wang, Q. Wang, and K. Q. Lu. Melting of superheated crystals initiated on vacancies. *Philos. Mag. Lett.*, 2007, 87, 19.